

Feedback from Winds and Supernovae in Massive Stellar Clusters. II: X-Ray Emission

H. Rogers and J.M. Pittard

School of Physics and Astronomy, The University of Leeds, Leeds, LS2 9JT

Received 17 February 2014. Accepted 31 March 2014

ABSTRACT

The X-ray emission from a simulated massive stellar cluster is investigated. The emission is calculated from a 3D hydrodynamical model which incorporates the mechanical feedback from the stellar winds of 3 O-stars embedded in a giant molecular cloud (GMC) clump containing $3240 M_{\odot}$ of molecular material within a 4 pc radius. A simple prescription for the evolution of the stars is used, with the first supernova explosion at $t = 4.4$ Myrs. We find that the presence of the GMC clump causes short-lived attenuation effects on the X-ray emission of the cluster. However, once most of the material has been ablated away by the winds the remaining dense clumps do not have a noticeable effect on the attenuation compared with the assumed interstellar medium (ISM) column. We determine the evolution of the cluster X-ray luminosity, L_X , and spectra, and generate synthetic images. The intrinsic X-ray luminosity drops from nearly 10^{34} ergs s^{-1} while the winds are ‘bottled up’, to a near constant value of 1.7×10^{32} ergs s^{-1} between $t = 1$ –4 Myrs. L_X reduces slightly during each star’s red supergiant (RSG) stage due to the depressurization of the hot gas. However, L_X increases to $\approx 10^{34}$ ergs s^{-1} during each star’s Wolf-Rayet (WR) stage. The X-ray luminosity is enhanced by 2–3 orders of magnitude to $\sim 10^{37}$ ergs s^{-1} for at least 4600 yrs after each supernova (SN) explosion, at which time the blast wave leaves the grid and the X-ray luminosity drops. The X-ray luminosity of our simulation is generally considerably fainter than predicted from spherically-symmetric bubble models, due to the leakage of hot gas material through gaps in the outer shell. This process reduces the pressure within our simulation and thus the X-ray emission. However, the X-ray luminosities and temperatures which we obtain are comparable to similarly powerful massive young clusters.

Key words: feedback – hydrodynamics – X-rays

1 INTRODUCTION

Massive stars have a profound affect on their natal environment. They have strong ionizing radiation fields which create HII regions, and their powerful winds sweep up surrounding material creating wind-blown shells and cavities. Their supernovae (SNe) chemically enrich the interstellar medium (ISM) and help to sustain turbulence within it. Thus the presence of massive stars in stellar clusters has implications for future generations of star formation. The dispersal and destruction of molecular material by the winds and ionizing radiation may inhibit further star formation within that region. Conversely, compression of material by winds and shocks may also trigger new star formation (Koenig et al. 2012) and new cluster formation (Beuther et al. 2008; Gray & Scannapieco 2011).

Many high-mass star-forming regions are observed to contain diffuse thermal X-ray emission, which requires high

temperature plasma. It has long been recognized that the fast winds of individual massive stars create high pressure and high temperature bubbles (e.g. Dyson & de Vries 1972; Castor et al. 1975; Weaver et al. 1977). In large clusters containing many early-type stars the individual stellar winds may combine, collectively creating a so-called cluster wind (e.g. Chevalier & Clegg 1985; Cantó et al. 2000; Stevens & Hartwell 2003).

In many cases the observed diffuse emission from massive-star forming regions (MSFRs) is relatively soft. For instance, in M17 and the Rosette nebula the characteristic temperature $kT < 1$ keV (Townsend et al. 2003). The X-ray emitting plasma in the Extended Orion nebula is similarly cool (Güdel et al. 2008). However, in other MSFRs the characteristic temperature is considerably higher. For instance, the diffuse thermal X-ray emission from NGC 3603 (Moffat et al. 2002), the core of the Arches

cluster (Wang et al. 2006), and the Quintuplet cluster (Law & Yusef-Zadeh 2004) has $kT > 2$ keV.

In some clusters the diffuse X-ray emission may be predominantly non-thermal: e.g. NGC 6334 (Ezoe et al. 2006a), RCW 38 (Wolk et al. 2002), the Arches cluster (Yusef-Zadeh et al. 2002; Wang et al. 2006) and ON2 (Oskinova et al. 2010). This requires non-thermal particles, which also occur when high speed flows and strong shocks are present. Townsley et al. (2011) argue that the non-thermal emission detected from the NGC 3576 OB association may arise from both a pulsar wind nebula and a cavity supernova. A caveat to some of these works is that the diffuse X-ray emission from clusters which are at larger distances is more likely to suffer contributions from unresolved point sources. A summary of X-ray studies of young stellar clusters is presented by Damiani (2010).

Early studies indicated that the detection of diffuse X-ray emission in stellar clusters required the presence of stars earlier than O6 (Townsley et al. 2003), although an exception, the O7-powered Hourglass nebula (Rauw et al. 2002), was known. Ezoe et al. (2006b) have since discovered diffuse X-ray emission from NGC 2024 (the Flame nebula), which contains only late O- to early B-type stars. On the other hand, it is curious that diffuse X-ray emission has yet to be detected from some very massive stellar clusters where very early O-type stars are present, such as Trumpler 16 (Wolk et al. 2011).

Other work has indicated that the temperature of the diffuse plasma may be correlated with how embedded it is, as measured by the column density (Ezoe et al. 2006a). Clusters with high temperature plasma appear to have $N_H > 5 \times 10^{21} \text{ cm}^{-2}$, while clusters with cooler plasma have less absorption. Wolk et al. (2008) suggest that while the stellar winds are bottled up the shocked gas remains maximally heated, but subsequent leakage and the resulting adiabatic cooling of the gas causes the gas temperature to drop.

Unfortunately, past comparisons of X-ray observations with theory have had mixed success. Many works on MSFRs simply compare the observed X-ray luminosity against the mechanical wind power of the stars, or the thermal energy of the plasma against an estimate of the time-integrated energy input of the winds (e.g. Townsley et al. 2003; Ezoe et al. 2006b; Güdel et al. 2008). The efficiency of the conversion of mechanical energy to radiation is then found to range from 10^{-4} to 0.1. This, and the estimated mass of the X-ray emitting gas, indicates that in many cases the winds are not completely confined and that hot plasma must flow into the wider environment. This conclusion is reinforced by the fact that the application of completely confined wind-blown-bubble models often leads to a significant overprediction of the X-ray luminosity (e.g. Rauw et al. 2002; Dunne et al. 2003; Harper-Clark & Murray 2009).

Other works have compared the X-ray luminosity and the surface brightness profile of the diffuse emission to the predictions of cluster-wind models. In their analysis of the Arches and Quintuplet clusters, Wang et al. (2006) found that the radial intensity profiles of the diffuse emission were more extended than theoretical predictions.

Harper-Clark & Murray (2009) recently determined that the observed diffuse X-ray emission from the Carina Nebula was 60 times too faint compared to predictions from the Castor et al. (1975) model, and 10 times too luminous

compared to the Chevalier & Clegg (1985) model. This led Harper-Clark & Murray to develop a third model whereby density variations in the ISM surrounding the cluster causes gaps in the swept-up shell, through which some of the high pressure gas in the bubble interior can leak. Their new model predicts a lower pressure within the bubble than the Castor et al. model, as the wind material is not completely confined, and also a lower X-ray luminosity. Consequently, it is more consistent with observations. However, since the covering fraction of the shell is a free parameter this model suffers from a lack of predictive power.

In young MSFRs in which there has not yet been time for any massive star to explode as a supernova, the diffuse X-ray emission must result from the action of stellar winds. However, in older clusters where some of the massive stars have exploded one still might not detect any signature of a SN explosion because the effect of a SNR on the thermal properties of the hot cluster gas is likely to be relatively short-lived. This time scale is generally believed to be $\sim 10^4$ yr (e.g. Kavanagh et al. 2011). For this reason, most studies of stellar clusters prefer a wind based explanation for the diffuse X-ray emission, though Ezoe et al. (2009) favour a recent SN explosion in their study of the Eastern Tip of the Carina nebula. A distinction exists between individual stellar clusters, and larger scale regions of star formation which create superbubbles where multiple cavity supernovae are believed to be responsible for the diffuse emission (such as those of 30 Doradus, e.g. Chu & Mac Low 1990; Townsley et al. 2011).

Given the challenges of interpreting such complex environments as MSFRs, and the highly idealized models of most theoretical and modelling work, in this paper the hydrodynamical models of stellar wind and supernova feedback in an inhomogeneous environment outlined in Rogers & Pittard (2013) (henceforth referred to as Paper I) are used as a basis to simulate the resulting X-ray emission from such regions. Of great interest are the X-ray luminosity and spectrum, and their temporal variation as the stars in the simulation cycle through various evolutionary stages, including main sequence, red supergiant, Wolf-Rayet and supernova. In Section 2 the details of the model and the method of calculating the X-ray emission and absorption are discussed. The results are presented in Section 3. Comparisons to numerical models and observations are made in Sections 4 and 5 respectively. Section 6 summarises and concludes this work.

2 SIMULATIONS

2.1 The Numerical Model

The X-ray calculations in this paper are based on the 3D hydrodynamical model described in Paper I. The simulations were performed using the hydrodynamical code ARWEN, which uses a piecewise parabolic interpolation and characteristic tracing to obtain the time-averaged fluid variables at each zone interface. An iterative Riemann solver is used to determine the time-averaged fluxes and solve the equations of hydrodynamics (see Paper I for more details). The simulations consist of three massive O stars which represent the main sources of mechanical feedback in a massive star forming region contained within an inhomogeneous

GMC clump of radius 4 pc and mass $3240 M_{\odot}$. The medium surrounding this clump is homogeneous, with a density of $3.33 \times 10^{-25} \text{ g cm}^{-3}$ ($n_H \approx n_e \approx 0.2 \text{ cm}^{-3}$) and a temperature of 8000 K. The simulations were performed on a 512^3 grid with free outflow boundary conditions. The total simulation volume covers a cubic region of ± 16 pc centered on the GMC clump. The cluster wind is injected as thermal energy within a radius of 6 cells (0.375 pc).

The evolution of the three stars is treated simplistically as three distinct phases - the Main Sequence (MS), Red Supergiant (RSG) and Wolf-Rayet (WR) phases. The details of the stellar cluster are summarized in Table 1. At the end of the Wolf-Rayet phase the stars explode imparting $10 M_{\odot}$ of material and 10^{51} ergs of thermal energy into the environment. The lifespans of the stars are designed in such a way so that there are three distinct supernova explosions over the course of the simulation.

The simulation utilizes a temperature dependent average particle mass, and molecular, atomic and ionized phases are tracked separately. The net heating/cooling rate per unit volume is parameterized as $\dot{e} = n\Gamma - n^2\Lambda$, where $n = \rho/m_H$. Γ is the heating coefficient and is set at a constant value of $\Gamma = 10^{-26} \text{ ergs s}^{-1}$. Λ is the cooling coefficient which is assumed to depend only on temperature. Cooling at low temperatures ($T \lesssim 10^4$ K) is then adjusted to provide three thermally stable phases which correspond to the molecular ($T \sim 10$ K), atomic ($T \sim 150$ K) and ionized ($T \sim 8500$ K) phases. This cooling curve and the phase diagram are shown in Pittard (2011). Photoevaporation is not treated in these simulations. However, as the photoevaporation time for a clump of these characteristics is comparable to the lifetime from ablation this should not significantly affect the results.

The simulations in Paper I showed that the inhomogeneous structure of the natal GMC cloud surrounding the cluster had an important effect on the initial expansion of the cluster wind, which cut channels through the low density material to escape the clump. The regions of high density within the initial clump proved to be surprisingly resistant to ablation from the cluster wind, and at later times the shockwaves of the SNRs.

2.2 Modelling the X-ray Emission and Absorption

To calculate the X-ray emission the results from the hydrodynamical model are read into a radiative transfer ray-tracing code, and the appropriate emission and absorption coefficients are calculated for each cell using the temperature and density values. A synthetic image on the plane of the sky is then generated by solving the radiative transfer equation along suitable lines of sight through the grid. Solar abundances and collisional ionization equilibrium are assumed throughout this work. The X-ray emissivity is calculated using the mekal emission code (Mewe et al. 1995, and references therein). The emissivity is stored in look-up tables containing 200 logarithmic energy bins between 0.1 and 10 keV, and 91 logarithmic temperature bins between 10^4 and 10^9 K. Line emission dominates the emissivity at temperatures below 10^7 K, with thermal bremsstrahlung dominating at higher temperatures. The present calculations also have an interstellar absorption column ($N_H = 10^{21} \text{ cm}^{-2}$) added to them, and each model is assumed to be at a distance of 1 kpc from an observer.

Table 1. Wind properties of the three stars in the cluster as they evolve.

Stellar			MS stage		
Mass (M_{\odot})	\dot{M} ($M_{\odot} \text{ yr}^{-1}$)	v_{∞} (km s^{-1})	Duration (Myr)	Mtm (kg m s^{-1})	Energy (ergs)
35	5.0×10^{-7}	2000	4.0	8.0×10^{36}	8.0×10^{49}
32	2.5×10^{-7}	2000	4.5	4.5×10^{36}	4.5×10^{49}
28	1.5×10^{-7}	2000	5.0	3.0×10^{36}	3.0×10^{49}
Stellar			RSG stage		
Mass (M_{\odot})	\dot{M} ($M_{\odot} \text{ yr}^{-1}$)	v_{∞} (km s^{-1})	Duration (Myr)	Mtm (kg m s^{-1})	Energy (ergs)
35,32,28	1.0×10^{-4}	50	0.1	1.0×10^{36}	2.5×10^{47}
Stellar			WR stage		
Mass (M_{\odot})	\dot{M} ($M_{\odot} \text{ yr}^{-1}$)	v_{∞} (km s^{-1})	Duration (Myr)	Mtm (kg m s^{-1})	Energy (ergs)
35,32,28	2.0×10^{-5}	2000	0.3	2.4×10^{37}	2.4×10^{50}

The energy bins are split into three energy bands which represent the soft, medium and hard X-ray components of the spectra. The soft X-ray regime runs from 0.1–0.5 keV, the medium runs from 0.5–2.5 keV and the hard X-rays run from 2.5–10.0 keV. These bands will be referred to as BB1, BB2 and BB3 respectively throughout this paper.

It should be noted that the individual stars are not resolved in the hydrodynamic simulations in Paper I, and therefore there is no contribution to the X-ray emission from the cluster wind interacting with any natal material close to the cluster (Parkin & Pittard 2010) or from intracluster wind-wind interactions (Cantó et al. 2000; Pittard & Parkin 2010).

3 RESULTS

3.1 The Main Sequence Phase

The X-ray lightcurve for the cluster throughout the simulation is shown in the top panel of Fig. 1. The initial observable luminosity of the cluster is $L_X \sim 7 \times 10^{31} \text{ ergs s}^{-1}$. Over the next 0.7 Myrs this luminosity decreases by a factor of 10 to approximately $L_X \sim 9 \times 10^{30} \text{ ergs s}^{-1}$, at which point it remains fairly constant for the duration of the MS of the cluster. Initially the X-ray luminosity is high as the cluster wind blown bubble is confined within the GMC clump. However, as the wind blows out of the low density regions of the clump, hot gas escapes from the centre, as described by the “leaky bubble” model of Harper-Clark & Murray (2009) and Paper I. The reduced pressure within the bubble caused by this leakage results in a lower X-ray luminosity.

Fig. 2 shows simulated X-ray images of the cluster at time $t = 0.13$ Myrs, where extended bubbles to either side indicate that some of the hot wind material is leaking from the GMC clump. However, it is clear that there is still partial confinement by the inhomogeneous GMC clump since the images are not spherically symmetric. At this time all three stars are on the MS (see Table 1 for the stellar properties). The left and middle panels show images of the soft

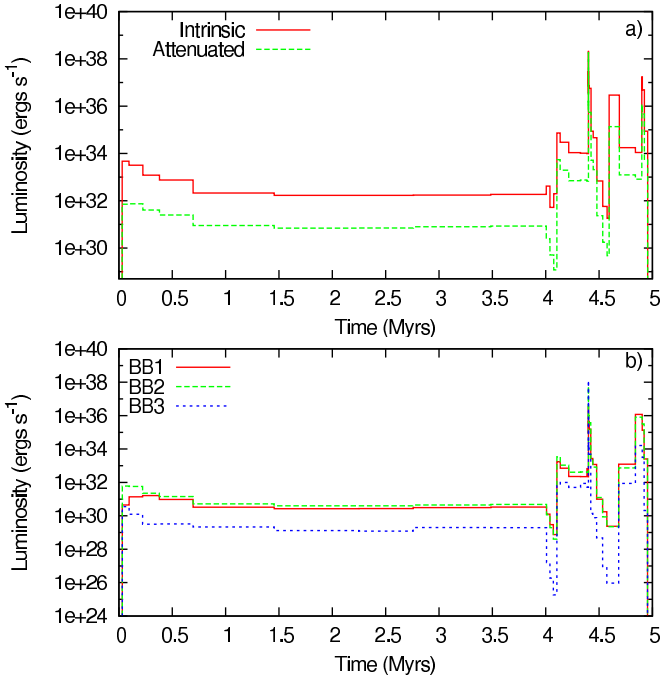


Figure 1. The X-ray lightcurve for the cluster over the course of the simulation. a) Shows the total intrinsic luminosity produced by the cluster (solid red line) compared with the observable luminosity after attenuation (dotted green line). b) Shows the attenuated luminosity in all three energy bands defined in Sec 2.2. The solid red line shows the soft X-rays in BB1, the green dashed line shows the medium X-rays in BB2 and the blue dotted line shows the hard X-rays in BB3.

and medium energy X-rays produced at this time, whilst the right panel shows the hard X-rays. The emission is brightest at the centre in all three images, but particularly so in the medium and hard images. At this early time there is strong absorption of the soft X-rays within the GMC clump, as revealed by the low surface brightness of regions which are more clearly emitting at higher energies (compare the left and middle panels). This behaviour is not so prominent in the medium energy X-ray image, although there is some absorption occurring.

The most striking feature in the images is the extended emission to the top right of the cluster, which results from the hot gas that has already broken out of the clump in this direction. It is also interesting to observe that the hot fluid adiabatically cools as it accelerates to supersonic speeds through the ‘nozzles’ from which it leaves the confining clump. This is visible as a reduction in the X-ray surface brightness in the hard band. The surface brightness of this gas increases at larger distances from the clump as it passes through a termination shock. At this point it runs up against previously shocked gas which is inflating the bubble and sweeping up a shell of the ambient medium which surrounds the GMC clump. The hardest X-rays are produced by the hot gas in the cluster centre, where the cluster wind is partially confined. The bottom panel of Fig. 1 shows that the luminosities in the BB1 and BB2 energy bands are almost equal during the period when all three stars are on the MS. However, at $t < 0.25$ Myrs the luminosity in the BB2 energy band is dominant due to the greater attenuation of the

lower energy X-rays by the remnant GMC clump. The hard X-ray luminosity in the BB3 energy band is about an order of magnitude lower than the luminosities in the soft and medium energy bands throughout the MS-dominated phase of the cluster evolution.

At $t = 0.13$ Myrs, approximately 90% of the total (0.1–10 keV) intrinsic X-ray luminosity originates from the inner 4 pc radius of the simulation, which is the original radius of the GMC clump containing the cluster. This is not unexpected as the cluster wind is young and hot plasma vents out of only a few open channels at this time. Since the GMC clump is mostly intact, significant attenuation of low energy X-rays occurs within the clump radius. This is reflected by the fact that only $\sim 2/3$ of the total attenuated luminosity originates from the inner 4 pc radius, indicating that the dense material within that radius has absorbed a substantial amount of the intrinsic emission.

The low density regions of the clump are rapidly blown out by the cluster wind but afterwards the remaining high density regions are much longer-lived. It should be noted that in simulations where there is hot, low density material in contact with cold, high density material minor heating of the cold dense gas may occur, and will be a function of the simulation resolution (Parkin & Pittard 2010). The effective covering fraction of the densest regions, the gross properties of the cluster wind and the X-ray luminosity evolve only slowly. However, the characteristic size of the emitting region continues to increase. Although much of the hot gas leaves the grid through the outflow boundaries, we can nevertheless examine how the emission from hot gas on the grid evolves with time. At $t = 0.44$ Myrs approximately 50% of both the intrinsic and attenuated luminosity originates from within the original clump radius. By $t = 1.96$ Myrs this value has decreased to 20% for both luminosities and by $t = 2.53$ Myrs, approximately midway through the MS, only 12% of the luminosity originating on the numerical grid comes from the central 4 pc radius. This decline is driven by two factors. First, the cluster wind increasingly clears out dense molecular gas within the original GMC clump as time goes on. The dense gas is both ablated into the hot gas streaming past and also pushed away. The bowshocks which form around the nearest dense clouds, and which merge to produce the reverse/termination shock of the cluster wind, thus form at greater and greater distances. Hence there is simply less hot gas in this central region as time increases. Secondly, the ablated material is entrained into the outflows away from the GMC clump. Indeed, mass entrainment/loading factors may exceed ~ 100 (see Section 3.4 in Paper I). This entrainment increases the density of the flow and its emissivity, while also creating slow moving obstacles which faster moving parts of the flow shock against. The flow outside of the GMC clump thus contains a multitude of shocks, and a wide range of densities and temperatures.

X-ray images of the cluster at $t = 2.53$ Myrs are shown in Fig. 3. There is considerable diffuse emission in the soft and medium X-ray bands (left and middle panels of Fig. 3). In contrast, the spatial extent of the hard X-rays is much smaller, and these instead primarily trace the stellar cluster and the hot, shocked gas immediately downstream of the reverse shock of the cluster wind. The gas responsible for this emission reduces in temperature as colder material from the remains of the GMC clump mixes in with it, which

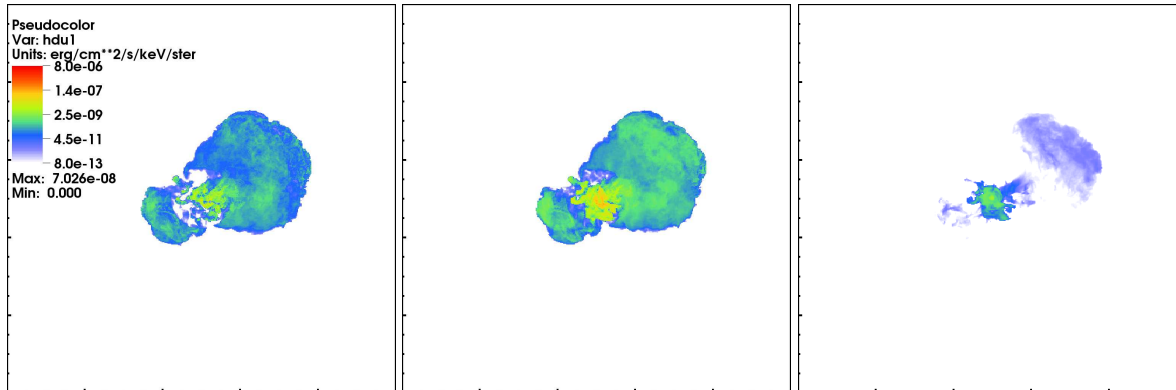


Figure 2. X-ray emission for the cluster at time $t = 0.13$ Myrs. Each panel has sides of 500 pixels and length 55.4 pc. [Left] shows soft X-rays 0.1–0.5 keV, [Middle] shows medium X-rays at 0.5–2.5 keV and [Right] shows hard X-rays at 2.5–10.0 keV. The stellar cluster is at the centre of each panel.

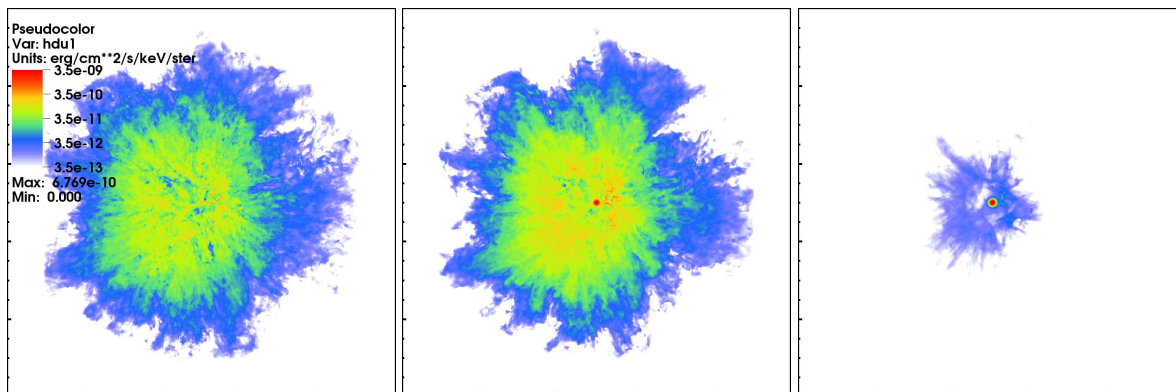


Figure 3. X-ray emission for the cluster at time $t = 2.53$ Myrs. Each panel has sides of 500 pixels and length 55.4 pc. [Left] shows soft X-rays 0.1–0.5 keV, [Middle] shows medium X-rays at 0.5–2.5 keV and [Right] shows hard X-rays at 2.5–10.0 keV.

limits the extent of the emission in this image. The extent of the diffuse emission reaches well beyond the original cluster radius, with more than 88% of the overall luminosity originating from outside that radius. Although the images for the soft and medium regimes are similar in structure, with strong emission in the centre and a filamentary diffuse structure towards the edges, there is a higher intensity in the BB2 image, and the stellar cluster is clearly discernable at the centre of the clump.

3.2 ISM Absorption Effects

The attenuated X-ray luminosity is dependent on both the ISM column density and the density and size of the GMC clump in which the cluster forms. However, as the molecular material in the clump is ablated by the winds it will have less of an effect on the observable luminosity of the cluster. Fig. 4 gives an indication of the degree of attenuation caused by the ISM and by dense clump material. The red solid line shows the intrinsic X-ray spectrum from the cluster, with the green dashed line showing the total attenuated spectrum taking all absorption effects into account. As discussed previously, the vast majority of the absorption occurs at soft X-ray energies, with very little occurring above $E = 1.0$ keV. The blue dotted line shows the attenuation effects caused only by absorption from the ISM. Close inspec-

tion of Fig. 4 reveals that the ISM absorption has little effect above 0.5 keV, whereas the circumcluster absorption affects the spectrum up to energies around 1 keV. Therefore it is clear that these two distinct absorption components affect the spectrum in slightly different ways. It is consistent with the hottest gas (and therefore the hardest emission) being buried more deeply within the GMC clump. We note that the average column density from the centre of the cluster through the GMC clump to an observer at $t = 0.06$ Myrs is, at $\approx 3 \times 10^{21} \text{ cm}^{-2}$ (see Fig.12 in Paper I), about 3 times the assumed ISM column.

At $t = 2.53$ Myrs (bottom panel of Fig. 4) the two attenuated spectra are practically identical. This is because the X-ray emitting gas is no longer confined by the dense absorbing material of the GMC clump as it is in the early stages of the bubble’s expansion, but now suffuses through the entire volume of the simulation. This is again consistent with the average column density from the centre of the cluster through the GMC clump to an observer at this time, which Fig.12 from Paper I shows to be about $10^{19.6} \text{ cm}^{-2}$, or only about 4% of the assumed ISM column.

Changing the viewing angle to the cluster at late times leads to only very small differences (≈ 5 –10%) in the attenuated luminosity, reinforcing the conclusion that the destruction of the clumpy environment results in very minimal column densities and thus attenuation by this gas. Even at

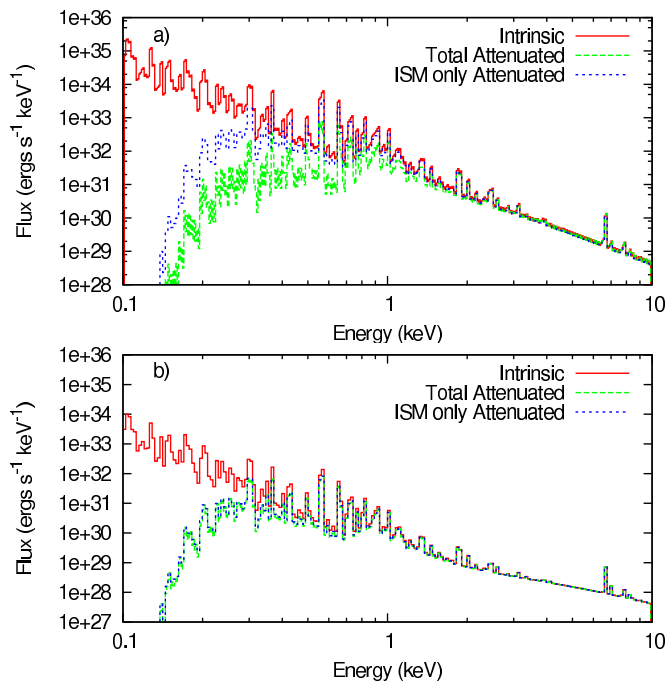


Figure 4. X-ray spectra of the cluster at two times during the MS dominated phase. The red solid line shows the total intrinsic emission produced by the cluster. The green dashed line shows the total observable emission after all attenuation effects are considered, whilst the blue dotted line shows the effect of just the ISM absorption on the emission. a) Shows the spectra at $t = 0.06$ Myrs, when there is a notable difference between the ISM only and total attenuated emission. b) Shows the spectra at $t = 2.53$ Myrs when absorption by dense material from the GMC clump has little effect on the overall attenuated emission.

earlier times when the hot wind gas is still breaking out of the clump the difference in the attenuated luminosity as the viewing angle to the cluster changes is only around 15–20%. This likely reflects the relatively low initial column density of the clump. Larger variations can be expected from models with higher initial column densities.

3.3 RSG and WR Phases for the $35 M_{\odot}$ Star

At $t = 4.0$ Myrs the most massive star evolves into a RSG. Its mass loss rate increases, and its wind velocity decreases. The averaged mass-loss rate and speed of the cluster wind then changes from $9 \times 10^{-7} M_{\odot} \text{ yr}^{-1}$ and 2000 km s^{-1} to $\approx 10^{-4} M_{\odot} \text{ yr}^{-1}$ and 136 km s^{-1} . The cluster wind therefore becomes slow and dense. The central cluster is no longer a source of hard X-rays, and there is no replenishment of the highest temperature gas in the surrounding environment as it flows away from the cluster through the remains of the porous GMC clump (see Fig. 8 in Paper I). Together these changes lead to a substantial reduction in the amount of hard X-rays being produced. In fact, the BB3 luminosity decreases 4 orders of magnitude from $L_X \sim 2 \times 10^{29} \text{ ergs s}^{-1}$ just before the evolutionary transition to $L_X \sim 2 \times 10^{25} \text{ ergs s}^{-1}$ by the end of the RSG phase (see Fig. 1). In contrast, the intrinsic luminosity briefly in-

creases following this transition, due to an increase in luminosity in the BB1 band.

Whilst the reason for this is not completely understood, it is possible that the sudden drop in pressure during the transition causes material stripped from the dense clouds to mix more rapidly with the hotter gas. Overall however, because the soft X-rays suffer from attenuation from the dense RSG-enhanced wind material close to the centre of the cluster, the attenuated emission actually drops.

The dense material deposited during the cluster wind's first RSG phase is subsequently cleared from the simulation volume once the most massive star further evolves to its WR phase at $t = 4.1$ Myrs. The combined average speed of the cluster wind increases back to 2000 km s^{-1} while the combined mass-loss rate becomes $2.04 \times 10^{-5} M_{\odot} \text{ yr}^{-1}$. The very high momentum that the cluster wind now has efficiently clears out the RSG dominated cluster wind filling the lower density channels and dramatically increases the ablation rate of the remaining dense clouds. This causes increased emission in all three X-ray bands. The intrinsic luminosity increases by over 2 dex above that reached in the MS phase, with an initial peak that then declines quickly to a steady value. This phase is relatively short-lived, lasting only 0.3 Myrs.

3.4 The First Supernova

The most massive star explodes as a supernova at $t = 4.4$ Myrs, imparting $10 M_{\odot}$ of ejecta and 10^{51} ergs of thermal energy into the centre of the GMC clump. At this point both of the other stars remain in their MS phases.

The X-ray lightcurve immediately following the supernova explosion is shown in Fig. 5. The SN ejecta is highly overpressured and rapidly expands into the surrounding medium. Although this approach leads to the desired response on the surrounding medium, in actual SN explosions the ejecta rapidly cools through adiabatic expansion, and is considerably cooler than the simulated ejecta at comparable times. Therefore the bright peak in the X-rays seen in Fig. 5 immediately after the explosion should be ignored as it is an artifact of the utilized approach. The X-ray luminosity of the hot ejecta drops rapidly from its peak as the ejecta starts to expand and its density decreases. However, Fig. 5 shows that the rate of decline of the X-ray luminosity decreases, and a minimum is reached after which the X-ray luminosity increases again. This behaviour is caused by ejecta running into the remaining dense clouds near the cluster. The kinetic energy that this ejecta has acquired at this time is then re-thermalized and subsequently radiates more strongly. The dashed line 900 yrs after the explosion indicates when the luminosity is dominated by the interactions of the ejecta with surrounding gas, and thus no longer affected by the explosion setup.

Synthetic X-ray images in all three energy bands during the explosion are shown in Figs. 6–8. When the star first explodes there is high intensity emission at the centre of the cluster, as seen in all three figures, which is a consequence of the implementation of the explosion with thermal rather than kinetic energy. As the hot ejecta expands outwards the intensity at the centre decreases, although it is still much higher than the pre-explosion levels.

Once the shockwave has expanded out far enough it be-

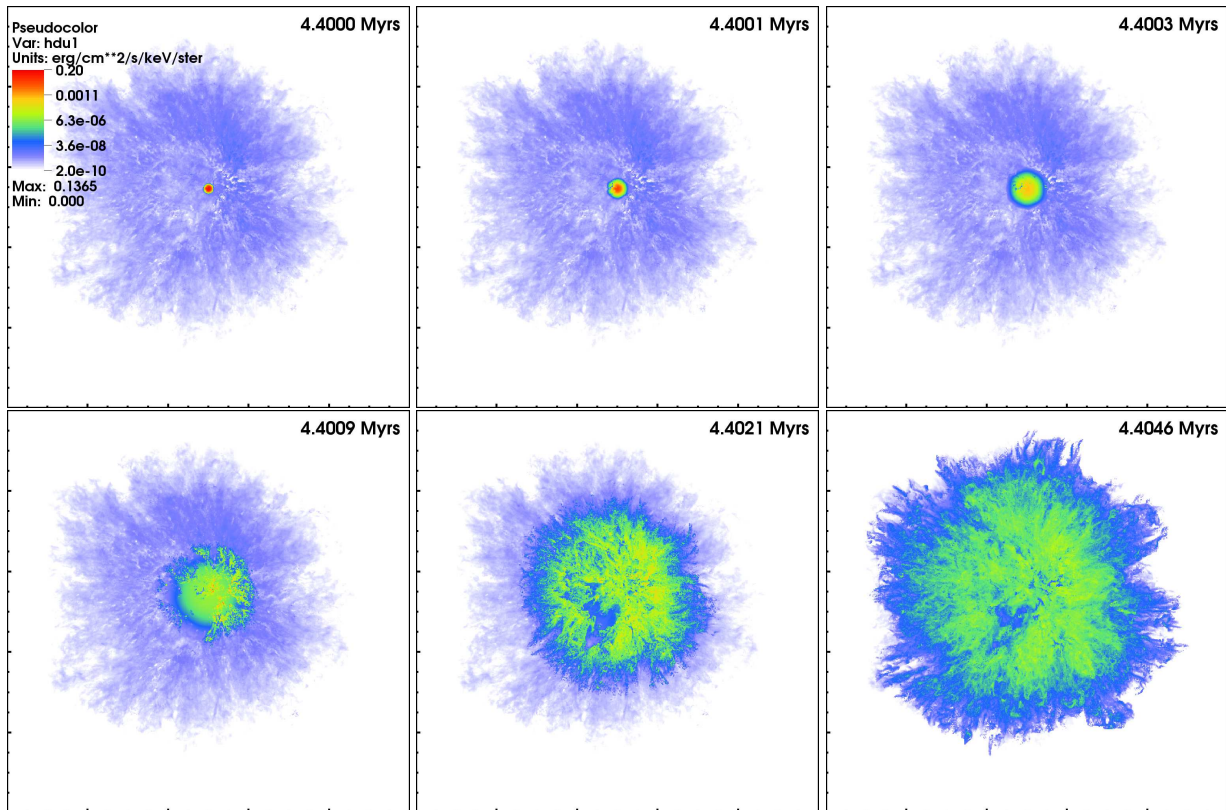


Figure 6. Synthetic X-ray image in the BB1 (0.1–0.5 keV) energy band during the first 4600 years after the most massive star explodes. The explosion occurs at $t=4.4000$ Myrs (top left panel). Absorption is visible from 100 years after the explosion. Bow shock emission dominates from 900 years.

gins to interact with the high density remains of the GMC clump. This is apparent from around $t = 4.4005$ Myrs onwards. Prior to this, absorption by dense clumps projected in front of the blast wave is visible (see for example the top middle and top right panels in Fig. 6). As the shockwave sweeps through the inhomogeneous environment successive bowshocks form around each dense cloud that it encounters. Individual bowshocks can be identified during the first 900 yrs after the explosion, but at later times these merge to create a single, though highly structured, region of emission with variable surface brightness. The simulated X-ray emission should be largely unaffected by the explosion setup once the emission from the bow shocks becomes dominant, which as is apparent from the previous discussion of the light curve occurs approximately 900 yrs after the explosion.

The X-ray image is broadly spherical overall, though there is substantial curvature to the main shock front on local scales. Ejecta begins to leave the grid approximately 4600 yrs after the explosion. By 2000 yrs after the explosion the most intense emission is observed somewhat behind the main shock front and the remnant takes on a “shell-like” morphology. This is likely due to the fact that at the time of the SN explosion the densest clouds surrounding the cluster tend to occur in a shell with inner and outer radii of ≈ 5 –10 pc. Virtually all of the dense gas previously within 5 pc has been cleared out by the cluster wind, being either ablated and entrained into the cluster wind or pushed away from the cluster by the ram pressure of the cluster wind up to a typical distance of 10 pc (see Fig. 7 in Paper I). The

brightest X-ray emission seems to occur where the SN ejecta interacts with the remaining dense clouds in this shell. In contrast, the position of the forward shock indicates where the SN ejecta has traversed relatively unimpeded through the surrounding medium.

The X-ray image appears to be smoother at the higher energies of BB3, and much more filamentary in the lower energies of BB1 and BB2, even near the edge of the forward shock front. The emission in BB1 and BB2 is likely picking up gas at relatively low and intermediate temperatures associated with material from dense clouds which is entrained into and partially mixed with the SN ejecta. Thus the resulting emission traces to some extent the interfaces associated with this process. However, this gas will be too cool to radiate strongly at the higher energies of the BB3 image, and instead the BB3 image shows the location of hot, but relatively unmixed ejecta.

The forward shock front also shows structures which could be interpreted as “blow-outs” (see for example the protrusion to the lower right of the SNR in the bottom right panel of Fig. 8). While these protrusions may indicate that the remnant is expanding into a region with a lower pre-shock density in this direction, it may also be affected by the structure of the surrounding medium that the shock front has encountered at distances considerably prior to this.

The X-ray emission from the environment external (and prior) to the SNR is also of interest. The emission at $t = 0.13$ Myrs and at $t = 2.53$ Myrs has already been displayed in Figs. 2 and 3, and discussed earlier. However,

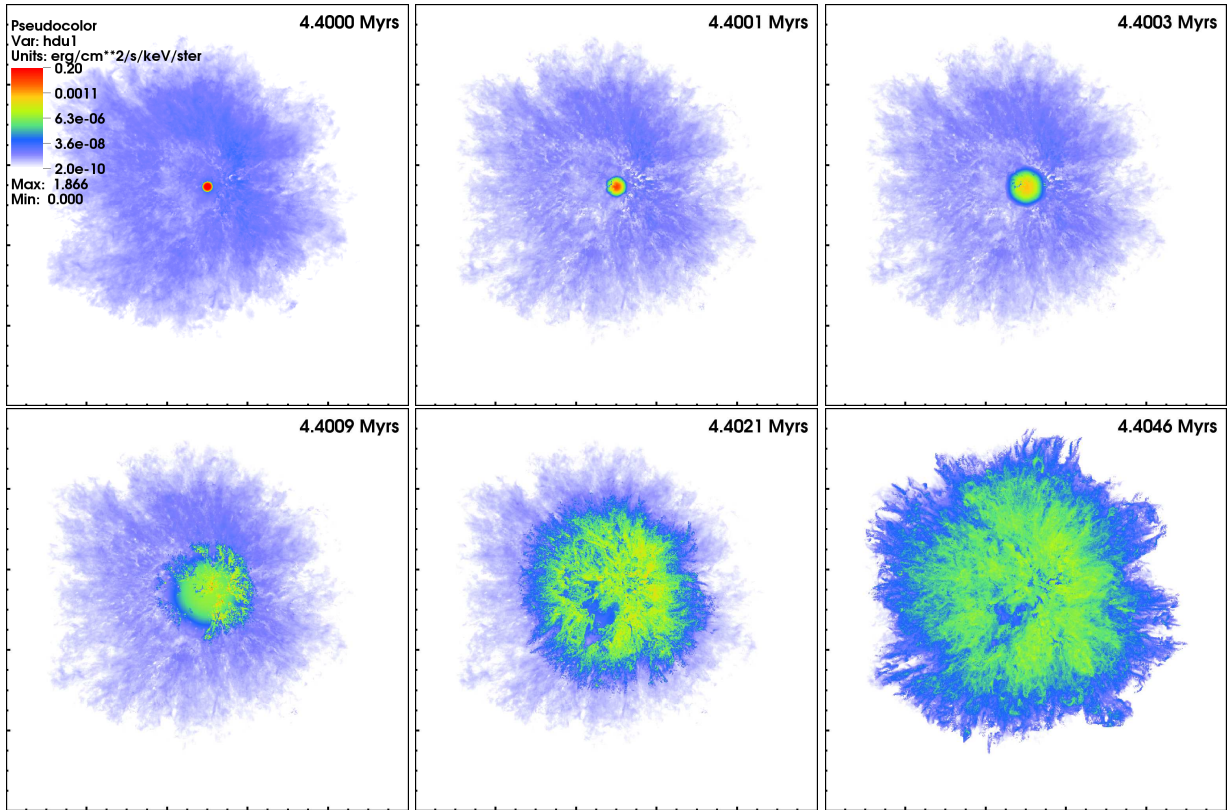


Figure 7. Same as Fig. 6, but for the BB2 (0.5–2.5 keV) energy band.

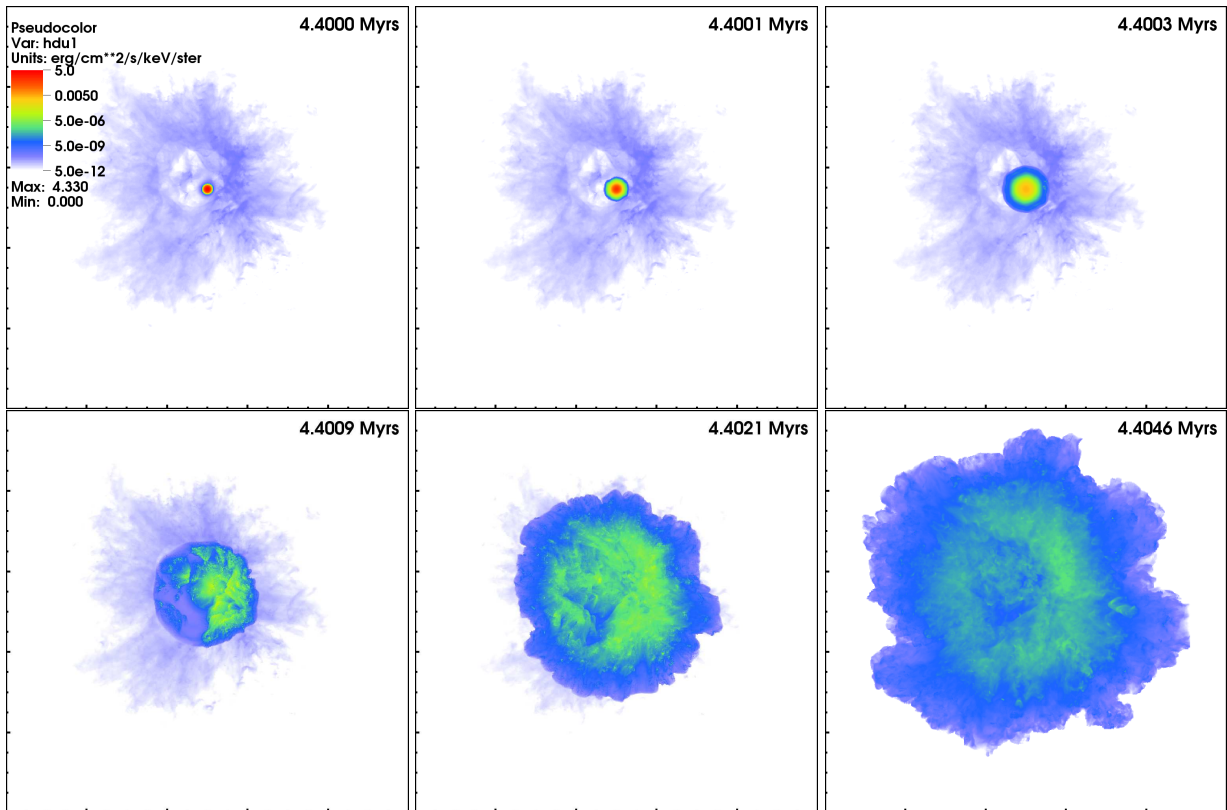


Figure 8. Same as Fig. 6, but for the BB3 (2.5–10.0 keV) energy band.

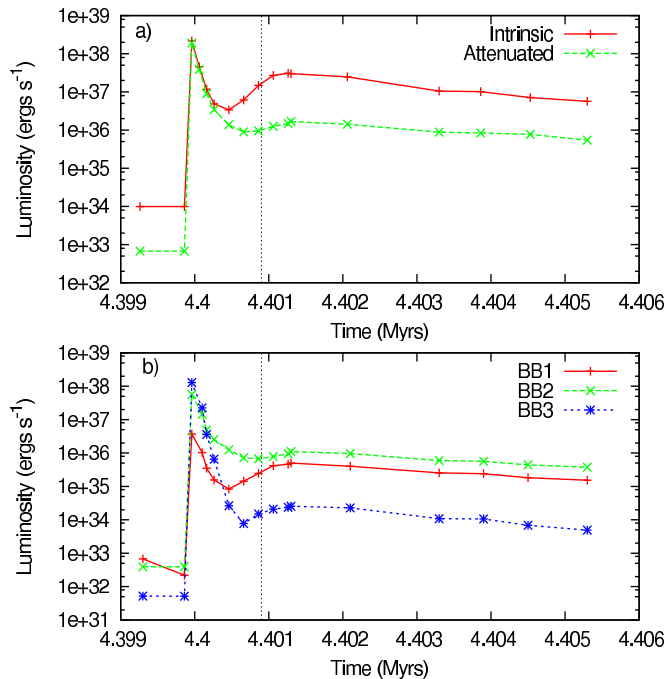


Figure 5. The X-ray light curve for the cluster at the time of the first SN explosion. The black dashed line indicates 900 years after the explosion, at which point emission from interactions with the surrounding clump material is dominant in all three energy bands. a) Shows the total intrinsic luminosity produced by the cluster (solid red line) compared with the observable luminosity after attenuation (green dashed line). b) Shows the attenuated luminosity in all three of the broadband energy bands. The solid red line shows the soft X-rays in BB1, the green dashed line shows the medium energy X-rays in BB2 and the blue dotted line shows the hard X-rays in BB3.

Figs. 6– 8 further illuminate the filamentary emission and absorption which occurs in the BB1 and BB2 energy bands, and the smoother emission which occurs in BB3. The volume within the reverse shock surrounding the stellar cluster is devoid of any hot gas and is visible as a deficit of emission in the central regions of Figs. 6 and 7. The highly structured nature of the reverse shock is directly visible in the top row of panels in Fig. 8. It is the X-ray bright parts of the top left panel in Fig. 8 which first “light-up” as the ejecta expands outwards. Bowshocks around the closest dense clouds to the cluster are responsible in both instances.

The time evolution of the attenuated spectra during the period of the first SN explosion is shown in Fig. 9. The solid red line is at a time just before the star explodes whilst the light blue dot-dashed line is $t = 4600$ yrs after the explosion, which is the approximate time at which the shockwave begins to leave the grid. The attenuated spectrum for the cluster at $t = 4.4009$ Myrs, when bowshock emission begins to dominate, is shown as the purple dotted line in Fig. 9. The spectrum is roughly the same shape, albeit considerably more luminous, as that of the pre-SN cluster. However, whilst the intensity of the soft and medium X-ray energies change little, by the time the ejecta reaches the edge of the grid (light blue dot-dashed line) there is a considerable decrease in the hard X-ray ($E \gtrsim 3$ keV) emission of the cluster.

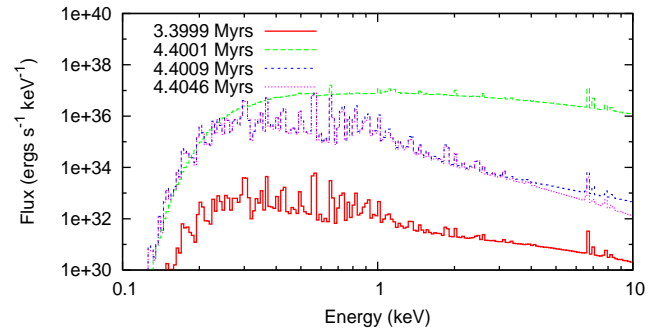


Figure 9. The time evolution of the attenuated X-ray spectra of the cluster as the most massive star undergoes a SN explosion. The solid red line is at a time just before the star explodes, the purple dotted line is ~ 900 yrs after the explosion and the light blue dot-dashed line is $\sim 4,600$ yrs after the explosion.

3.5 Further Evolutionary Stages

After the $35 M_{\odot}$ star has exploded the remaining two stars continue in their MS phases for a further 0.1 Myrs, at which point the $32 M_{\odot}$ star begins to follow the same evolutionary path as its predecessor. At $t = 4.5$ Myrs it evolves to a RSG and at $t = 4.6$ Myrs it becomes a WR star. The X-ray lightcurve shown in Fig. 1 shows a similar pattern to the previous evolution, in that the X-ray luminosity decreases once the less powerful RSG wind contributes to the cluster wind, while it increases once the star becomes a WR. However, as the evolution of the $32 M_{\odot}$ star occurs so shortly after the first supernova, the luminosity is still declining from the aftermath of that event, partially as a consequence of the blast wave leaving the grid, and so it is hard to distinguish this from the natural decline during the RSG phase. In fact, the luminosity at this stage is comparable to that of the previous RSG phase despite the loss of one wind source and the commensurate reduction in the momentum and energy flux of the cluster wind. The $32 M_{\odot}$ star explodes at $t = 4.9$ Myrs, imparting a further $10 M_{\odot}$ of ejecta and 10^{51} ergs of energy into the simulation. 0.1 Myrs after this explosion the final remaining star begins the evolutionary sequence already performed by its brethren.

3.6 Properties of the X-ray Emitting Gas

The mass, volume and density of the X-ray emitting gas are shown in Table 2. The mass of gas with a temperature in excess of 10^5 K increases until $t \approx 0.3$ Myr when it stands at nearly $7 M_{\odot}$. The mass then drops slightly and stays around $3-4 M_{\odot}$ during the remaining MS phase of the cluster wind. During this time the X-ray emitting volume is just over 50% of the total simulation volume, since the shocked cluster wind has spread throughout most of the grid. The average temperature of the X-ray emitting gas is 2.5×10^6 K, whilst the mass-weighted average is 2.3×10^5 K, implying that most of the X-ray emitting gas is closer to the 10^5 K mark. After the first star evolves to the RSG branch the mass of material which is hot enough to produce X-rays decreases along with both the average and the mass-weighted average temperature of the gas. Once the star evolves further to the WR phase the mass of X-ray producing gas increases by a factor of 10 and the volume of the material at $T > 10^5$ K almost

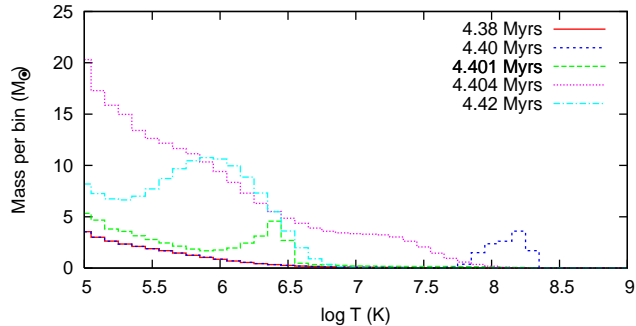


Figure 10. Mass of X-ray emitting material above $T = 10^5$ K at five times during the simulation. The red solid line is at $t = 4.38$ Myrs, shortly before the most massive star explodes. The blue short-dashed line is at $t = 4.40$ Myrs immediately after the supernova explosion (this reflects the conditions used to simulate the explosion) and the green long-dashed line is at $t = 4.401$ Myrs, 1000 yrs after the explosion when the emission is dominated by bowshock interactions. The purple dotted line is at $t = 4.404$ Myrs when the ejecta begins to leave the grid. The light blue dot-dashed line is at $t = 4.42$ Myrs, 20,000 yrs after the explosion. Each temperature bin is of width 0.1 dex.

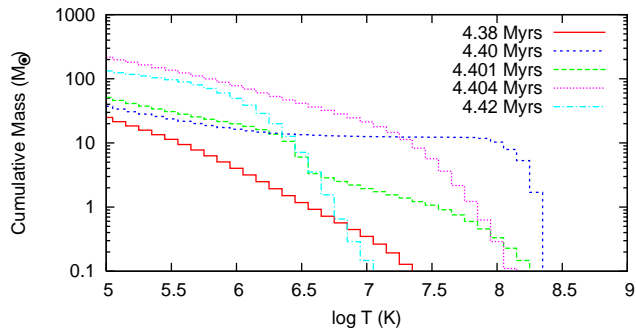


Figure 11. Shows the cumulative mass of X-ray emitting material above $T = 10^5$ K at five times throughout the simulation. The red solid line is at $t = 4.38$ Myrs, shortly before the most massive star explodes, the blue short-dashed line is at $t = 4.40$ Myrs immediately after the SN explosion. The green long-dashed line is at $t = 4.401$ Myrs at which point bowshock emission becomes dominant, and the purple dotted line is at $t = 4.404$ Myrs, when SN ejecta begins to leave the grid. The light blue dot-dashed line is at $t = 4.42$ Myrs, 20,000 yrs after the explosion.

doubles. The average temperature of the X-ray emitting gas increases to 2.8×10^6 K and the mass-weighted average to 3.2×10^5 K.

The mass distribution of the simulation before, during and after the first supernova explosion is shown in Fig. 10, and the amount of material which is at each temperature above 10^5 K is shown in Fig. 11. The red line shows the temperature distribution of the $25 M_\odot$ of material above 10^5 K shortly before the explosion at $t = 4.38$ Myrs. There is virtually no gas at temperatures greater than 10^7 K ($0.35 M_\odot$, see the red line in Fig. 11), and the mass-weighted average temperature is $T_{av} = 3.2 \times 10^5$ K. The SN occurs at $t = 4.40$ Myrs, and its hot ejecta is visible as the short-dashed blue line in Figs. 10 and 11. As discussed previously, bowshock emission from the SN becomes dominant approximately 900 yrs after the explosion. The temperature distri-

bution of the $51 M_\odot$ of material above 10^5 K at this time is shown by the green long-dashed line in Figs. 10 and 11. There is a small amount of material above 10^7 K ($\sim 2 M_\odot$), but the majority of the material is between $10^5 - 10^{6.5}$ K, after which there is an obvious decrease in X-ray emitting material. The mass-weighted average temperature is $T_{av} = 5.9 \times 10^5$ K at this time.

The SN ejecta begins to leave the grid at $t = 4.404$ Myrs, shown as the purple dotted line in Figs. 10 and 11. There is approximately $218 M_\odot$ of material above 10^5 K at this time (see Table 2), with $\sim 10\%$ ($21 M_\odot$) of that material above 10^7 K. 20,000 yrs after the explosion there is again virtually no gas at $T > 10^7$ K as the shock heated gas slowly cools (shown by the light blue dot-dashed line in Fig. 10). However, there is approximately 5 times more material between $10^5 - 10^7$ K than before the supernova, with a peak at about $T = 10^6$ K. Fig. 11 also reveals that the maximum temperature of gas at $t = 4.42$ Myrs is actually lower than that at $t = 4.38$ Myrs, at $T_{max} = 10^{7.4}$ K and $T_{max} = 10^{7.7}$ K respectively.

4 COMPARISON TO 1D BUBBLE MODELS

4.1 Wind-Blown Bubble Models

Chu et al. (1995) derived an analytical expression for the X-ray emission from a Weaver et al. (1977) wind-blown bubble (WBB), in terms of various physical parameters which are observable, such as the density and size of the bubble. The predicted X-ray luminosity in the 0.1–2.4 keV band is:

$$L_X = (1.1 \times 10^{35} \text{ erg s}^{-1}) \xi I(\tau) L_{37}^{33/35} n_0^{17/35} t_6^{19/35} \quad (1)$$

where ξ is the metallicity relative to the solar value, L_{37} is the mechanical luminosity of the stellar wind(s) in units of $10^{37} \text{ erg s}^{-1}$, n_0 is the number density of the ambient medium in cm^{-3} and t_6 is the age of the bubble in 10^6 yr . The above equation contains a dimensionless temperature τ , where the dimensionless integral $I(\tau) = (125/33) - 5\tau^{1/2} + (5/3)\tau^3 - (5/11)\tau^{11/2}$ and $\tau = 0.16 L_{37}^{-8/35} n_0^{-2/35} t_6^{6/35}$.

At $t = 0.3$ Myrs the expected luminosity in the 0.1–2.4 keV energy band as predicted using Equation 1 is $L_X \approx 2.06 \times 10^{35} \text{ erg s}^{-1}$ using the average ambient density of the mostly intact GMC clump of $n_0 \approx 250 \text{ cm}^{-3}$. This compares to the combined luminosity from our BB1 and BB2 energy bands, which at $L_X = 3.9 \times 10^{31} \text{ erg s}^{-1}$ is roughly 5000 times lower than the prediction from the standard Weaver et al. (1977) bubble. Because the edge of the bubble expands off the grid at $t \sim 0.2$ Myrs, we will have somewhat underestimated the true luminosity of our simulation, but it is clear that a large discrepancy nevertheless remains.

By $t = 2.53$ Myrs the destruction of the GMC clump is well advanced and we should clearly reduce our estimate of the appropriate value for the ambient density, n_0 . Using an estimate of the density as $n_0 \approx 0.3 \text{ cm}^{-3}$ (which is just 50% greater than the low density medium which surrounds the GMC clump in the simulations), the predicted X-ray luminosity from Equation 1 would be $L_X \approx 1.4 \times 10^{34} \text{ erg s}^{-1}$. Although our simulation only ‘‘captures’’ a small proportion

Table 2. The mass, density and volume of the X-ray emitting gas, and the average and mass-weighted average temperature of that gas at various times throughout the simulation.

Time (Myrs)	Phase of each star (35,32,28 M_{\odot})	Mass at $T > 10^5$ K (M_{\odot})	Density at $T > 10^5$ K ($\times 10^{-26}$ g cm $^{-3}$)	Volume at $T > 10^5$ K ($\times 10^4$ pc 3)	% of Volume at $T > 10^5$ K	$\log[T_{\text{av}}]$ at $T > 10^5$ (K)	Mass-weighted $\log[T_{\text{av}}]$ at $T > 10^5$ K (K)
0.00	MS,MS,MS	0.00	0.00	0.00	0.00 %	6.40	5.58
0.13	MS,MS,MS	1.89	5.17	0.25	7.63 %	6.40	5.44
0.32	MS,MS,MS	6.75	3.22	1.43	43.53 %	6.40	5.36
0.63	MS,MS,MS	4.26	1.60	1.81	55.28 %	6.40	5.37
0.95	MS,MS,MS	3.25	1.20	1.83	55.92 %	6.40	5.37
1.95	MS,MS,MS	3.43	1.33	1.75	53.32 %	6.40	5.39
2.53	MS,MS,MS	3.84	1.41	1.85	56.46 %	6.40	5.28
3.61	MS,MS,MS	4.06	1.42	1.95	59.40 %	6.40	5.51
4.06	RSG,MS,MS	2.13	1.08	1.34	40.89 %	6.40	5.51
4.31	WR,MS,MS	24.87	6.64	2.55	77.82 %	6.40	6.36
4.38	WR,MS,MS	24.99	6.69	2.54	77.54 %	6.80	5.77
4.40	SN,MS,MS	37.24	9.87	2.57	78.43 %	6.80	5.83
4.4009	SN,MS,MS	51.29	13.64	2.56	78.09 %	6.80	5.86
4.404	SN,MS,MS	217.97	52.67	2.82	85.95 %	6.45	5.77
4.41	MS,MS	231.57	53.04	2.97	90.64 %	6.20	5.29
4.42	MS,MS	132.53	29.94	3.01	91.92 %	6.40	5.52
4.56	RSG,MS	1.69	2.51	0.46	14.04 %	7.00	5.86
4.78	WR,MS	28.53	9.07	2.14	65.31 %	6.35	5.58
4.90	SN,MS	37.61	10.66	2.40	73.24 %		
4.94	MS	81.54	21.05	2.64	80.57 %		

of the X-ray luminosity at this time since a lot of the hot gas has flowed through the grid boundaries, the estimate from Equation 1 is approximately 2000 times larger than the luminosity from our simulations at this time. Since this factor is likely to be many times greater than the “true” X-ray luminosity from our simulation (i.e. the luminosity we would infer if our grid were big enough to contain the expanding bubble), we conclude that Equation 1 consistently overestimates the X-ray luminosity produced from our simulations by a large margin.

Harper-Clark & Murray (2009) also provide an analytical expression for the expected X-ray luminosity of a Weaver wind-blown-bubble:

$$L_X \sim 3 \times 10^{38} \xi \left(\frac{L_w}{4 \times 10^{38} \text{erg s}^{-1}} \right)^2 \left(\frac{20 \text{pc}}{r} \right)^3 \left(\frac{6 \times 10^6 \text{K}}{T} \right)^4 \cdot \left(\frac{3.6 \times 10^6 \text{yr}}{t} \right)^2 \quad (2)$$

where they have assumed an X-ray cooling rate $\Lambda_X \approx 3 \times 10^{-23} \xi \text{erg s}^{-1} \text{cm}^3$ and t is the age of the cluster/wind source. Applying this expression to the Carina nebula overestimates the observed luminosity by a factor of 10^4 (Harper-Clark & Murray 2009). In the following we apply Equation 2 to our simulated cluster at a time when the stars are on their MS phases and the mechanical luminosity of the cluster wind is $L_w = 1.16 \times 10^{36} \text{erg s}^{-1}$. The average temperature of the X-ray emitting gas at $t = 2.53$ Myrs is 2.5×10^6 K (see Table 2). We only capture a small part of the bubble volume at this time. However, we can be guided by what an observer may choose as the bubble radius. If the ISM column to the cluster was substantially higher than our assumed value of 10^{21}cm^{-2} , the emission below 2.5 keV may be almost completely absorbed, in which

case Fig. 3 shows that only the harder emission might be detected. The radius that an observer might then infer for the “bubble” in the BB3 image in Fig. 3 could then be approximated to 6 pc. This leads to a predicted X-ray luminosity of $L_X \approx 10^{36} \text{erg s}^{-1}$ using Equation 2, and an overestimate of the intrinsic emission “captured” in our simulation by roughly 4 orders of magnitude. To bring the values from Equation 2 in line with the simulated results would require a bubble radius of 130 pc.

Clearly some of the underlying assumptions made in these equations are incompatible with the simulated results. The two main assumptions in the Weaver et al. bubble model which differ from our simulations are that the energy deposited by the stellar winds is confined within the bubble and that the surrounding ISM is homogeneous. As discussed in both Harper-Clark & Murray (2009) and Paper I, leakage of hot gas from the bubble interior leads to a significant reduction in the pressure. This in turn reduces the X-ray luminosity so that it is well below that from a confined bubble (c.f. Harper-Clark & Murray 2009). It is interesting that the calculated X-ray luminosity from our simulations is roughly 3–4 dex lower than the predictions from the confined bubble model, which is of order of the same difference between observations of real clusters and the confined bubble model.

4.2 Cluster Wind Models

Chevalier & Clegg (1985) and Cantó et al. (2000) derived an analytical model describing the cluster wind flow that results from the multiple interactions of the stellar winds produced by the stars of a dense cluster of massive stars. Rodríguez-González et al. (2007) developed the work of Cantó et al. (2000) to include a non-uniform stellar distribution.

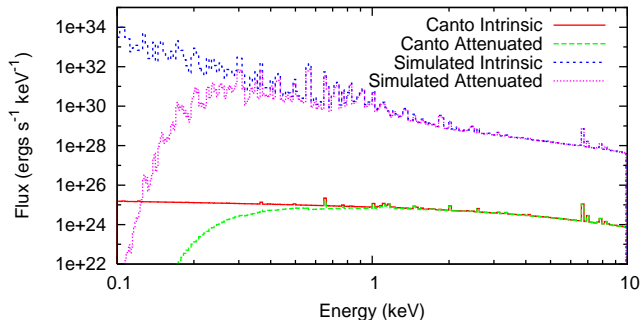


Figure 12. A comparison between the intrinsic and attenuated X-ray spectrum of our simulated cluster whilst all three stars are on the MS with the Cantó et al. (2000) analytical cluster wind model. The red solid line shows the intrinsic and the green long-dashed line shows the attenuated X-ray luminosity as calculated from the Cantó et al. model.

In order to compare these models with the simulations presented in this work, the cluster mass-loss rate and the average velocity were set to $\dot{M}_{\text{cl}} = 9 \times 10^{-5} M_{\odot} \text{ yr}^{-1}$ and $v_{\text{cl}} = 2000 \text{ km s}^{-1}$ respectively, equivalent to the simulated cluster at a time when all three of the stars are still on the MS (see Table 1 for the individual stellar properties). The cluster radius in both of the analytical models was set to $R_{\text{cl}} = 0.04 \text{ pc}$, which is consistent with stellar clusters of comparable mass. The X-ray spectrum of these solutions are shown in Fig. 12, along with the X-ray spectrum of our simulated cluster at $t = 2.53 \text{ Myrs}$.

It is clear that the Cantó et al. (2000) model produces X-ray luminosities significantly lower than from our simulated cluster. This is expected considering the lesser degree of confinement of the stellar winds inherent in the cluster wind model (c.f. Harper-Clark & Murray 2009).

5 COMPARISONS TO OBSERVATIONS

5.1 Young Massive Stellar Clusters

It is widely observed that there is a deficit of X-ray emission from stellar clusters compared with predictions based on the WBB model of Weaver et al. (1977) (Dorland et al. 1986; Dorland & Montmerle 1987; Oey 1996; Rauw et al. 2002; Dunne et al. 2003; Smith et al. 2005; Harper-Clark & Murray 2009). Many explanations of this effect have been suggested, for example lower stellar luminosities, mass or energy loss from the bubble, or highly efficient mass loading which reduces the temperature of the cluster below X-ray temperatures. However, mass-loading may also produce higher X-ray luminosities (Stevens & Hartwell 2003). Section 4 demonstrated that the X-ray luminosities produced by the model in Paper I also exhibit a lower luminosity than predicted by WBB models. A comparison will now be made between our model results and observations of M17 and the Rosette Nebula. For a full literature review of young massive stellar clusters from which diffuse X-ray emission has been detected see Table 3 and Appendix A.

5.1.1 M17

M17 is a young blister HII region located on the northeast edge of one of the largest GMCs in the Galaxy, at an approximate distance of 1.55 kpc. It is estimated to be only $\sim 0.5 \text{ Myrs}$ old (Chini & Hoffmeister 2008; Hoffmeister et al. 2008). M17 is photoionized by the massive stellar cluster NGC 6618, within which Broos et al. (2007) have identified 14 O-stars. An earlier study by Hanson et al. (1997) identified at least 9 O-stars and a few late-O/early-B stars.

The diffuse X-ray emission from M17 has previously been analyzed by Dunne et al. (2003), Townsley et al. (2003), Hyodo et al. (2008), and most recently by Townsley et al. (2011). The total X-ray luminosity is thought to be $L_X = 2 \times 10^{34} \text{ ergs s}^{-1}$. At $t = 0.44 \text{ Myrs}$, the simulated cluster has an intrinsic 0.1–10 keV luminosity (BB1+BB2+BB3) of $L_X = 7.48 \times 10^{32} \text{ ergs s}^{-1}$, approximately 25 times lower than in M17. However, given the number and type of O-stars in M17, the difference in emission from our simulated cluster and the observed X-ray luminosity from M17 can be considered to be perfectly acceptable. Townsley et al. (2003) estimate the mass of plasma at $T \sim 10^6 \text{ K}$ to be $0.3 M_{\odot}$. Whilst the simulated cluster has $4.26 M_{\odot}$ at $t = 0.63 \text{ Myrs}$ (see Table 2), this includes gas at temperatures greater than $T > 10^5 \text{ K}$. The amount of material at temperatures above 10^6 K in our simulated cluster is actually $0.31 M_{\odot}$ at this time, which is remarkably similar to the observations of M17. For more information on M17 see Appendix A.

5.1.2 Rosette Nebula

The Rosette Nebula is a blister HII region at the tip of the giant Rosette molecular cloud. It is estimated to be $\sim 2 \text{ Myrs}$ old (Hensberge et al. 2000). A study carried out by Martins et al. (2012) identified 7 O-stars in the cluster NGC 2244 contained within the Rosette Nebula. The earliest spectral type so far detected is O4V((f)).

Townsley et al. (2003) find that soft diffuse X-ray plasma surrounds the OB association and fills the nebula cavity completely. This plasma likely originates from the O star winds and is later brought to thermalization by wind-wind interactions or by shocking against surrounding molecular material. They estimate the mass of the diffuse plasma at $T > 10^6 \text{ K}$ to be $M_X \sim 0.05 M_{\odot}$, which is again much lower than in our simulated cluster at this time ($3.43 M_{\odot}$, see Table 2). However, the amount of X-ray emitting material above $T > 10^6 \text{ K}$ in our simulated cluster is actually $0.3 M_{\odot}$, and above $T > 10^7 \text{ K}$ it is $0.02 M_{\odot}$. These values are a much better match to the observations of the Rosette Nebula.

The intrinsic 0.5–2 keV luminosity is $\approx 7 \times 10^{32} \text{ ergs s}^{-1}$, with no significant emission detected above 2 keV. At $t = 1.96 \text{ Myrs}$, our simulated cluster has an intrinsic 0.5–2.5 keV luminosity (BB2) of $L_X = 6.46 \times 10^{30} \text{ ergs s}^{-1}$. Given the higher mass-loss rate of the Rosette cluster ($\dot{M}_{*} = 2.5 \times 10^{-6} M_{\odot} \text{ yr}^{-1}$, Stevens & Hartwell 2003) and the higher number of O-stars present, this is a reasonably close match to the simulations. For more information on the Rosette Nebula see Appendix A.

Table 3. The properties of young massive stellar clusters from which diffuse X-ray emission has been detected. The clusters are ordered roughly by age. The abbreviation “CF” in column 4 is short for champagne flow. Further details and references for values in this table can be found in Appendix A.

Cluster/Region Name	Age (Myr)	Distance (kpc)	X-ray Morphology	Thermal/NT	L_X (erg s^{-1})	kT (keV)	N_H (cm^{-2})
RCW 38	$\lesssim 1$	1.7	CF/blowouts	NT	3×10^{32}	0.2	9.5×10^{21}
Omega (M 17)	~ 0.5	2.0	CF/blowout	T	2×10^{34}	0.28,0.29,0.57	$1.6, 5, 10 \times 10^{21}$
Westerlund 2	$\lesssim 2$	2.85 ± 0.43	CF	T	4.6×10^{33}	0.1,0.8,3.1	$4, 12, 12 \times 10^{21}$
Rosette	2	1.55	CF	T	7×10^{32}	0.06,0.8	2×10^{21}
Hourglass	1–2.5	1.3	CF	T	$\lesssim 6.6 \times 10^{32}$	0.63	1.1×10^{22}
Arches	2–2.5	8	CF	T (+NT)	3.8×10^{33}	2.56	1.1×10^{23}
NGC 2024 (Flame)	0.3–3	0.415	CF	T	2×10^{31}	11	$0.21, 3.3 \times 10^{22}$
Orion (M 42)	3	0.49	CF	T	5.5×10^{31}	0.17	$4.1 (< 1.0) \times 10^{22}$
Quintuplet	3.5–4	8	CF	T	3×10^{33}	$10^{+4.6}_{-2.7}$	3.8×10^{22}
NGC 3603	1–4	7 ± 1	CF	T	2.6×10^{35}	0.53	2×10^{22}
Westerlund 1	4–5	4–5	CF	T (+NT?)	$1.7\text{--}30 \times 10^{33}$	0.7,3.0	2×10^{22}
NGC 3576N		2.8 ± 0.3	CF	T (+NT)	5.9×10^{33}	0.11,0.5,0.67	$0.3, 1.3 \times 10^{22}$
NGC 3576S		2.8 ± 0.3	Blowout	T	1.1×10^{34}	0.31,0.53	$1.3, 0.3 \times 10^{22}$

5.2 Young SNRs from Core-Collapse SNe

When the stars in the simulation explode they input $10 M_\odot$ of material and 10^{51} ergs of energy into the surroundings. As seen in Fig. 5 the results of this explosion should only be trusted after 900 yrs when the dominant source of X-ray emission is from interactions between the blast wave and the surrounding clumpy medium. The ejecta begins to leave the grid after 4600 years, at which point hot gas and its corresponding emission begins to be lost. A comparison will now be made between the model and observations of young SNRs which are of age $900 < t < 4600$ years. Four SNRs matching these criteria are identified, as noted in Table 4. Each of these are now discussed in turn.

5.2.1 1E0102.2-7219

1E0102.2-7219 (hereafter 1E0102) is a SNR in the Small Magellanic Cloud (SMC) with an inferred kinematic age of ~ 2100 yrs (Eriksen et al. 2001) at a distance of ~ 60 kpc (Wada et al. 2013). The progenitor is thought to have been a Wolf-Rayet star with a zero-age MS (ZAMS) mass of $\sim 32 M_\odot$ that underwent significant mass loss prior to exploding as a Type Ib/c or IIL/b supernova. Gaetz et al. (2000) used *Chandra* to image the SNR, finding it to be almost “textbook”, with a hotter outer ring surrounding a cooler, denser inner ring which is likely the reverse-shocked stellar ejecta. The diameter of the SNR was estimated to be 40” by Hughes (1988) (approximately 12 pc at 60 kpc distance). More recently, Hughes et al. (2000) estimated the radius of the blast wave to be 6.4 pc, in good agreement with their earlier work. Hughes et al. (2000) also estimated an expansion age of ~ 1000 yrs, though Eriksen et al. (2001) disagree, deriving a free expansion age of 2100 yrs. However, recently Wada et al. (2013) have proposed that the source is a Be/NS binary. There is little interstellar extinction along the line of sight to 1E0102 which allows a comprehensive, multi-wavelength analysis from the X-ray to the radio domain.

Hughes et al. (2000) estimated the expansion velocity of the blast wave to be 6000 km s^{-1} based on a radius of

6 pc and an age of 1000 yrs, although Flanagan et al. (2004) find from Doppler shifts that the majority of the bulk matter is moving at a lower 1000 km s^{-1} . Hughes et al. (2000) also estimate the temperature in the postshock region to be 0.4–1.0 keV. Gaetz et al. (2000) estimated the upper limit on X-ray emission of the central source to be $< 9 \times 10^{33} \text{ ergs s}^{-1}$, whilst Wada et al. (2013) estimate the 0.5–10 keV luminosity of the Be/NS binary to be $\sim 8.8 \times 10^{35} \text{ ergs s}^{-1}$ using Suzaku data. This is only a factor of 2 lower than our intrinsic 0.5–10 keV X-ray emission from the simulated cluster, which is $L_X = 1.53 \times 10^{36} \text{ ergs s}^{-1}$ and $L_X = 1.69 \times 10^{36} \text{ ergs s}^{-1}$ for 1000 and 2000 yrs after the first SN explosion respectively. As the simulation assumes collisional ionization equilibrium (CIE), which is unlikely to be the case in 1E0102, it is not surprising that higher luminosities are obtained from the simulation. The clumpy environment in the simulated cluster may also be partially responsible, if the environment of 1E0102 has lower density and/or is more homogeneous. The expansion velocity of the simulated blast-wave is between $\sim 6000\text{--}8000 \text{ km s}^{-1}$ (see Table 4), which although high is similar to the estimate of the blast wave by Hughes et al. (2000).

5.2.2 MSH 11-54

Also known as G292.0+1.8, this is a core-collapse SN with an estimated age of 2700 - 3200 years (Chevalier 2005; Winkler et al. 2009; Tanaka & Takahara 2013), and a distance of 6 kpc (Gaensler & Wallace 2003). It is one of a handful of O-rich SNRs known today (Park et al. 2007; Ghavamian et al. 2012). The X-ray emission from such O-rich SNRs is thought to arise from faster, non-radiative shocks in lower density ejecta and interstellar gas. The central source is thought to be a pulsar wind nebula. The SNR has a radius of approximately 15 pc assuming a distance of 6.2 kpc (Gaensler & Wallace 2003).

Gonzalez & Safi-Harb (2003) derived an average temperature for the SNR using two components - a high temperature plasma associated with the supernova blast wave and a low temperature plasma from the reverse shock. These two components were estimated to be 1.05 ± 0.34 and 0.37

Table 4. Young SNRs from core-collapse SNe compared with the simulated results. The SNRs are ordered roughly by age. References can be found in the accompanying text in §5.2. Five sets of simulation results are given, spanning the estimated age range of the observed SNRs.

SNR Name	Alternative Name	L_x (ergs s $^{-1}$)	Diameter (pc)	Age (yr)	V_{exp} (km s $^{-1}$)	Temperature (keV)	Distance (kpc)	Prog. Mass (M_{\odot})
1E0102.2-7219		$\sim 8.8 \times 10^{35}$	~ 12	$\sim 1000\text{--}2100$	1000	2.5–4.5,0.4–1	60	32
MSH 11-54	G292.0+1.8	$> 7.2 \times 10^{32}$	15	2700–3200	$\lesssim 1200$	1.05,0.37	< 6	20-40
N 132D	SNR 0525-69.6	$4.5\text{--}7.5 \times 10^{37}$	$\sim 20\text{--}25$	3150	2250–3700	0.6–0.7	55	30-35
Puppis A		1.2×10^{37}	~ 32	3700–4450	> 1500	0.6	1.3-2.2	> 25
Simulation		2.71×10^{37}	~ 18	1060	~ 5900	0.68	1	35
Simulation		2.49×10^{37}	~ 27	2060	~ 5200	0.68	1	35
Simulation		1.67×10^{37}	~ 29	2630	~ 1600	0.68	1	35
Simulation		1.05×10^{37}	~ 30	3300	~ 1000	0.54	1	35
Simulation		1.02×10^{37}	~ 31	3860	~ 1000	0.54	1	35

± 0.18 keV respectively. The progenitor star is estimated to have had a mass of 30–40 M_{\odot} , though Hughes & Singh (1994) estimated a lower mass of 20–25 M_{\odot} . A more recent estimate of the temperature by Park et al. (2007) using *Chandra* data found a highly non-uniform distribution of hot, X-ray emitting gas in the remnant ranging from kT \sim 5 keV in the NW regions to around kT \sim 0.7 keV in the SE. These results are a promising match with our results 2000–3300 years after the explosion of the 35 M_{\odot} star, when the average temperature of the X-ray emitting plasma is $\simeq 0.54\text{--}0.68$ keV. The SN explosion producing MSH 11-54 is thought to have been asymmetric, which would explain the spatial variation of temperatures and the greater expansion of the remnant towards the NW. Hughes et al. (2003) found the unabsorbed 0.3–10 keV X-ray luminosity of the central pulsar to be $L_X = 7.2 \times 10^{32}$ ergs s $^{-1}$, but made no estimate for the entire remnant. Our simulated cluster at around this time has a total 0.1–10 keV intrinsic luminosity of $L_X \sim 1 \times 10^{37}$ ergs s $^{-1}$.

5.2.3 N132D

N132D is one of the brightest SNRs in the Large Magellanic Cloud (LMC) and has an estimated age of 3150 years (Morse et al. 1995) and an inferred progenitor mass of 30–35 M_{\odot} (Blair et al. 2000). With a diameter of 80", the distance to the SNR of approximately 55 kpc (Hughes 1987) implies a real diameter of ~ 21 pc. This is a similar estimate to the extent of the X-ray shell, which has an estimated radius of 12 pc (Morse et al. 1995). The expansion velocity of the SNR has been estimated by several authors (e.g. Morse et al. 1995; Hwang et al. 1992), with values ranging from 2250–3700 km s $^{-1}$. In comparison, the radius of our simulated SNR at around 3300 yrs after the explosion is ~ 15 pc, with an inferred expansion velocity of ~ 4400 km s $^{-1}$.

The X-ray luminosity in the 0.2–4 keV energy band was estimated by Hughes (1987) to be $4.5\text{--}7.5 \times 10^{37}$ ergs s $^{-1}$, based on thermal plasma temperatures of $10^{6.8} - 10^{7.1}$ K and a hydrogen column density of $10^{21} - 10^{21.5}$ cm $^{-2}$ (Raymond & Smith 1977). The estimated luminosity is actually higher than the simulated results ($L_X = 1.05 \times 10^{37}$ ergs s $^{-1}$ at 3300 yrs), despite the fact that the simulations assume CIE. However, given the inherent differences

in the simulated and actual environments these results can be considered a reasonable match. The plasma temperature is very similar to that found in the other SNRs mentioned, at approximately 0.6–0.7 keV, compared with an average of 0.54 keV from our simulated remnant (see Table 2). There is patchy X-ray absorption around the remnant thought to be caused by gas just outside the molecular cloud towards the northern tip of N132D (Kim et al. 2003).

5.2.4 Puppis A

Puppis A is a nearby Galactic SNR and has age estimates ranging from 3700 yr (Winkler & Kirshner 1985) to 4450 yr (Becker et al. 2012), making it most comparable to the simulation 3900 yrs after the explosion (see Table 4). A distance of 2.2 kpc has been estimated based on HI and CO studies (Reynoso et al. 2003), although a closer distance of 1.3 kpc has also been proposed by Woermann et al. (2000) based on OH line detections. This remnant is embedded in a complex region composed of large atomic and molecular clouds and an interstellar density gradient. The remnant is about 50' in diameter (approximately 32 pc at a distance of 2.2 kpc). A progenitor mass of 25 M_{\odot} was inferred by Canizares & Winkler (1981).

Optical knots detected from Puppis A are evident only in the northeast, implying the ejection of the matter during the explosion was asymmetric (Katsuda et al. 2008). Oxygen-rich filaments are detected to have radial velocities higher than ~ 1500 km s $^{-1}$. These filaments are interpreted as SN ejecta which have remained mostly uncontaminated by the ISM (Winkler & Kirshner 1985).

Recently, Dubner et al. (2013) studied Puppis A using *Chandra* and XMM-Newton. They estimated the X-ray luminosity between 0.3 and 8.0 keV to be $L_X = 1.2 \times 10^{37}$ ergs s $^{-1}$ assuming a distance of 2.2 kpc. The X-ray emission from Puppis A appears to be dominated by the swept-up ISM due to very low metal abundances (Hwang et al. 2008). The total intrinsic X-ray luminosity of our simulated remnant 3860 yrs after the explosion is $L_X = 1.02 \times 10^{37}$ ergs s $^{-1}$, which is a reasonable match to Puppis A.

The average temperature in the remnant is 0.6 keV, very similar to the average temperature of 0.54 keV seen in the

simulated remnant at 3860 years after the explosion (see Table 2).

6 CONCLUSION

This paper investigates the X-ray emission from a massive young stellar cluster embedded in an inhomogeneous GMC clump treating only the mechanical effects from winds and supernovae. The hydrodynamical input model was previously simulated in Paper I, and this work explores the emission arising from that model. Initially the dense parts of the clump decrease the observed X-ray emission due to attenuation, but once the cluster wind has destroyed and ablated a large portion of this material the attenuation from the ISM material is dominant.

At very early times, when the wind material is still confined by the inhomogeneous GMC material the X-ray luminosity is reasonably bright, at $L_X \approx 5 \times 10^{33} \text{ ergs s}^{-1}$. However, as the cluster wind erodes and destroys the surrounding clump it is no longer completely confined and therefore hot gas is able to leak through the gaps in the shell. This causes a reduction in the X-ray luminosity as the pressure within the bubble decreases. Once the low density gas from the clump has been ablated away the covering factor of the cluster remains more or less constant, leading to an approximately constant intrinsic X-ray luminosity of $1.7 \times 10^{32} \text{ ergs s}^{-1}$ and an attenuated X-ray luminosity of $7 \times 10^{30} \text{ ergs s}^{-1}$.

The most massive star becomes a RSG at $t = 4.0 \text{ Myrs}$, resulting in a large drop in the X-ray luminosity in all three of the X-ray broadbands studied. The most dramatic decrease is seen in the BB3 (2.5–10.0 keV) emission, where the attenuated X-ray luminosity drops four orders of magnitude, from $L_X \sim 2 \times 10^{29} \text{ ergs s}^{-1}$ to $L_X \sim 2 \times 10^{25} \text{ ergs s}^{-1}$ by the end of the RSG phase. The drop in X-ray luminosity in the other two broadbands over this period is around a factor of 50 and 100 for BB1 (0.1–0.5 keV) and BB2 (0.5–2.5 keV) respectively. Although a lot of material is deposited in the RSG-enhanced cluster wind, the amount of material at X-ray emitting temperatures is very low, contributing to the lack of X-ray emission observed at this time.

100,000 years later the most massive star further evolves to become a WR star, causing a dramatic increase in X-ray emission in all three broadband regions studied. The amount of material at a temperature greater than 10^5 K increases by an order of magnitude over that seen in the RSG stage, and a total of 78% of the computational volume contains X-ray emitting material. The high momentum cluster wind sweeps up the slower moving material deposited in the previous phase and heats it to high temperatures, with the average temperature of hot gas ($T > 10^5 \text{ K}$) at this time being around $T = 2.5 \times 10^6 \text{ K}$. The total attenuated X-ray emission increases to $L_X \sim 5 \times 10^{33} \text{ ergs s}^{-1}$, which is about 30 times greater than that observed when all three stars were on the MS.

At $t = 4.4 \text{ Myrs}$ the most massive star in our simulation explodes as a SN, ejecting $10 M_\odot$ of material and 10^{51} ergs of energy into the simulation. Due to the way in which the explosion is initialised, the emission from the SNR only becomes independent of the initial conditions of the explosion once the interaction of the blastwave with the surrounding

material becomes dominant. In this work this occurs approximately 900 years after the explosion. The ejecta begins to leave the grid 4600 years after the explosion, and therefore the emission from the SNR can be compared with observations of SNRs only between the ages of $900 < t < 4600$ years.

The supernova of the $35 M_\odot$ star was compared with four young core-collapse SNe with ages ranging from ~ 1000 – 4450 yrs . Although collisional ionization equilibrium was assumed in our simulation, which is unlikely to be true for such young remnants, we find that the X-ray luminosity and electron temperatures are reasonable matches to observational results reported in the literature. Unfortunately, as the ejecta begins to leave the grid 4,600 yrs after the initial explosion no comparisons can be made with older remnants.

The simulated emission from the cluster during the wind-dominated phases is substantially lower than predicted by 1D spherically symmetric WWB calculations, but is higher than predicted by cluster wind models. The fact that our simulations fall between these two models ties in very nicely with the theory of leaky bubble models, where the WWB is only partially confined. The simulated results match reasonably well to actual observations of several massive young stellar clusters. This is likely to be due the assumptions made in these calculations being overly simplified compared to the simulated model. Firstly, the assumption that the hot wind material is confined within a bubble is very much not the case, and a reduction in the pressure in the simulated cluster leads to a reduction in the X-ray luminosity. The surrounding density is not homogeneous as described in these models, which will lead to local areas of confinement and leakage. Clearly the highly complex environment of young massive star forming regions requires similar complexity in simulations in order to better understand their properties.

ACKNOWLEDGEMENTS

HR acknowledges a Henry Ellison Scholarship from The University of Leeds and JMP acknowledges funding from the Royal Society for a University Research Fellowship and from the STFC. We would also like to thank the referee for their timely and useful comments.

APPENDIX A: NOTES ON INDIVIDUAL STELLAR CLUSTERS

A1 RCW 38

RCW 38 is a very young ($< 1 \text{ Myr}$), highly embedded ($A_V \sim 10$), and close ($D = 1.7 \text{ kpc}$) stellar cluster surrounding a central pair of O5.5 stars (IRS 2) (e.g. Winston et al. 2011). The dominant IRS 2 stars have cleared a region completely free of dust out to a radius of 0.1 pc . The extinction is patchy, and the HII region appears to be breaking out of the surrounding molecular gas in some directions. Extended warm dust is found throughout a $2 - 3 \text{ pc}$ region and coincides with extended ($1.25 \times 1.75 \text{ pc}$) X-ray plasma which is predominantly non-thermal (Wolk et al. 2002). The power-law index of the emission steepens toward the cluster core.

Contamination of the diffuse emission by unresolved point-sources is not significant at distances of more than 0.15 pc (~ 15 arcseconds) from the cluster center, though may be responsible for the more thermal nature of the diffuse emission measured in the core (Wolk et al. 2006). The cause of the non-thermal emission remains unclear.

The diffuse emission is strongest in the central core near IRS 2, and is confined on the southeast along a ridge. Recent *Spitzer* observations reveal that winds from IRS 2 have caused outflows towards the northeast, northwest and southwest of the central cluster (see e.g. Fig. 4 in Winston et al. 2012).

An excellent review of this cluster is given in the Handbook of Star Formation, where the luminosity of the diffuse X-ray emission is given as about 3×10^{32} ergs s^{-1} (Wolk et al. 2008).

A2 The Omega Nebula (M17)

M17 is a very young blister H II region located on the northeast edge of one of the largest giant molecular clouds in the Galaxy, with an extent of 4° (~ 110 pc, Elmegreen et al. 1979). The geometry of M17 is thought to resemble the Orion Nebula HII region except that it is seen edge-on rather than face-on (Meixner et al. 1992; Pellegrini et al. 2007). M17 is photoionized by the massive stellar cluster NGC 6618, which has 14 identified O stars (Broos et al. 2007), and is estimated to be ~ 0.5 Myr old (Chini & Hoffmeister 2008; Hoffmeister et al. 2008). The distance has recently been determined using trigonometric parallax to be 2.0 kpc (Xu et al. 2011). Several obscured O4-O5 stars form a central 1 arcminute ring in NGC 6618, and are principally responsible for ionizing the nebula. Extinction is patchy ($A_V = 3 - 15$ with an average of 8 to the OB stars, though some parts of the cluster have $A_V > 20$, Hanson et al. 1997). The earliest O stars are an O4+O4 visual binary known as Kleinmann's Anonymous Star (Kleinmann 1973), which may in fact be a pair of colliding wind binaries (Broos et al. 2007; Hoffmeister et al. 2008; Rodríguez et al. 2012). Evidence for an older (2 - 5 Myr) stellar population to the North is presented by Povich et al. (2009).

The diffuse X-ray emission from M17 has previously been analyzed by Dunne et al. (2003), Townsley et al. (2003), Hyodo et al. (2008), and most recently by Townsley et al. (2011). It has relatively high surface brightness and blows out to the east of the cluster, extending nearly 10 pc from the cluster. The plasma appears to be channelled by the famous northern and southern ionization bars (Povich et al. 2007), and maintains roughly constant temperature as it flows (Townsley et al. 2003; Hyodo et al. 2008). Although obscuration changes across the field, a global fit to the diffuse emission with a 3-temperature NEI model yields $kT_1 = 0.28$, $kT_2 = 0.29$ and $kT_3 = 0.57$ keV, with the highest temperature component providing 56% of the intrinsic luminosity (Townsley et al. 2011). The absorption to each of these emission components increases with the temperature of the component, so that the kT_3 component suffers 6 times as much obscuration as kT_1 . There are indications that the shocked gas is not in complete ionization equilibrium, which is suggestive of it recently being shocked. Several gaussian lines are also needed - the cause is

speculated to be charge exchange processes. The total X-ray luminosity is 2.0×10^{34} erg s^{-1} .

Townsley et al. (2003) previously determined that the X-ray plasma had a mass of $0.15 M_\odot$, which when rescaled to a distance of 2.1 kpc becomes $0.3 M_\odot$ (for an assumed distance D , $V_x \propto D^3$, $L_x \propto D^2$, $n_{e,x} \propto (L_x/V_x)^{1/2} \propto D^{-1/2}$, and $M_x \propto n_{e,x} V_x \propto D^{5/2}$). Townsley et al. (2003) determine that $n_{e,x} \sim 0.3 \text{ cm}^{-3}$. The analysis by Hyodo et al. (2008), which does not quite include the most easterly extent of the plasma, is generally consistent with the earlier work of Townsley et al. (2003), except for the determination of a significantly lower plasma temperature of ≈ 0.25 keV.

A3 Westerlund 2 (RCW 49)

Westerlund 2 (hereafter W2) is a compact young open cluster embedded in and responsible for the luminous HII region RCW 49. W2 contains at least a dozen OB stars. Two WR stars, WR20a and (especially) WR20b, lie outside the cluster core (see references in Churchwell et al. 2004). W2 is also located in the direction of one of the Galaxy's strongest sources of γ -rays (Aharonian et al. 2007; H.E.S.S. Collaboration et al. 2011). The distance to W2 has been very difficult to pin down, with estimates ranging from 2 to more than 8 kpc in the literature, but a new study puts it at 2.85 ± 0.43 kpc, and determines an age of no more than 2 Myr (Carraro et al. 2013).

Diffuse X-ray emission from W2 was identified in a *Chandra* observation (Townsley et al. 2005). The emission is brightest at the core of W2, and extends preferentially towards the west. The emission can be fitted with a 3-temperature thermal plasma model with $kT_1 = 0.1$, $kT_2 = 0.8$ and $kT_3 = 3.1$ keV, with the highest temperature component providing 30% of the intrinsic luminosity (Townsley et al. 2005). Assuming a distance of 2.3 kpc, the absorption corrected 0.5-8 keV luminosity is $L_x = 3 \times 10^{33}$ erg s^{-1} . At $D = 2.85$ kpc, this increases to $L_x = 4.6 \times 10^{33}$ erg s^{-1} . The absorbing column to kT_1 is less than the identical columns to kT_2 and kT_3 . The hardest thermal component is not well constrained, and replacing it with a power-law component ($\Gamma = 2.3$) also gives an acceptable fit. The diffuse flux will be slightly underestimated due to the use of a 5 arcmin radius extraction region and a nearby on-chip background region.

More recently diffuse emission has also been analyzed from a *Suzaku* observation (Fujita et al. 2009). The *Chandra* pointing was used to determine the point source contamination to the *Suzaku*-derived diffuse emission, and the central region ($r < 2$ arcmin) was masked out. The diffuse emission is found to extend to an 8 arcminute radius. The spectral analysis is broadly consistent with the earlier results of Townsley et al. (2005).

A4 The Orion Extended Nebula (M42)

The Orion Nebula Cluster (ONC), also known as the Trapezium cluster, contains the nearest rich and concentrated sample of pre-MS stars. The OB members of the ONC photoionize the Orion Nebula (M42), a blister HII region at the near edge of Orion A, the nearest giant molecular cloud ($D \approx 450$ pc). Güdel et al. (2008) recently detected diffuse, soft (0.3 - 1 keV) X-ray emission in the Extended

Orion Nebula (EON). The characteristic temperature of the plasma is $kT \approx 0.2$ keV. The intrinsic X-ray luminosity in the 0.1 – 10 keV energy band is $L_x = 5.5 \times 10^{31}$ ergs s⁻¹. Two regions of diffuse emission, a northern and a southern, are identified with respective emission measures of $EM = n_e^2 V = 1.5 \times 10^{54}$ and 1.9×10^{54} cm⁻³. The attenuating column N_H is very low, being 4.1×10^{20} cm⁻² for the northern, and $< 10^{20}$ cm⁻² for the southern.

The total mass of the X-ray emitting gas is estimated to be $0.07 M_\odot$, which is roughly 10^5 yrs of mass-loss of the dominant O5.5 star θ^1 Ori C. The radiative cooling time is estimated to be $\approx 1.8 - 3.9$ Myr. The density of the X-ray plasma is determined to be $n_e = 0.1 - 0.5$ cm⁻³. The X-ray and ionized gas are in approximate pressure equilibrium ($n_{\text{HII}} \approx 100$ cm⁻³), and the hot gas is likely channeled by the cooler denser structures rather than disrupting them by expansion. Leakage of the hot plasma via an X-ray champagne flow into the nearby Eridanus superbubble is suggested.

A5 The Rosette Nebula

The Rosette Nebula is a blister HII region at the tip of the giant Rosette molecular cloud. It has a distinct ring-like appearance in both radio and optical images, and is photoionized by the open cluster NGC 2244 whose stellar winds have cleared a hole in the Nebula's centre (Celnik 1985; Townsley et al. 2003). NGC 2244 contains 7 O-type stars, all of which have MS luminosity classes, with the earliest spectral type being O4V((f)). A recent analysis of 6 of these stars by Martins et al. (2012) determined an upper age limit of 2 Myr for the most massive stars, in excellent agreement with earlier determinations (e.g. Hensberge et al. 2000; Park & Sung 2002). Photometric distance estimates range between 1.4 and 1.7 kpc, and 1.55 kpc is adopted in this work. Wang et al. (2008) find an absence of mass segregation and conclude that the cluster is not dynamically evolved. The two dominant O stars (HD 46223, O4V((f)); HD 46150, O5V((f))z) are widely separated (by at least 3 pc). In contrast, the O stars in the Trapezium Group and M17 are concentrated within the inner 0.5 pc.

Townsley et al. (2003) find that soft diffuse X-ray plasma surrounds the OB association and fills the nebula cavity completely. It likely originates from the O-star winds which are thermalized by wind-wind interactions or by shocking against surrounding molecular material. The X-ray emission is brightest in the central 3 pc radius, corresponding roughly to the central cavity. The diffuse emission can be fit by a two-temperature thermal plasma model, with components $kT_1 = 0.06 \pm 0.02$ and $kT_2 = 0.8 \pm 0.1$ keV and a single absorbing column $N_H = 2 \pm 1 \times 10^{21}$ cm⁻². The hotter component is dominant. The intrinsic 0.5 – 2 keV luminosity (for $D = 1.55$ kpc) is $\approx 7 \times 10^{32}$ ergs s⁻¹. There is no significant emission above 2 keV. Correcting Townsley et al.'s values for a slightly greater assumed distance, the diffuse plasma number density and mass are estimated as $n_{e,x} \sim 0.1$ cm⁻³ and $M_x \sim 0.05 M_\odot$.

A6 The Quintuplet Cluster

The Quintuplet cluster is named after its five brightest stars (Nagata et al. 1990). It is located near the Galactic Centre,

is unusually dense, and is host to at least 10 massive, windy, WR stars and more than a dozen luminous OB supergiants (Figer et al. 1999a,b). It is somewhat less massive and dense than the Arches cluster, however. Its age is estimated to be about 3.5 – 4 Myr (Figer et al. 1999b; Liermann et al. 2012).

Law & Yusef-Zadeh (2004) determine that the Quintuplet cluster shows thermal diffuse emission with a peak temperature $kT = 2.42 \pm 0.5$ keV at the cluster centre, and with $L_x \sim 10^{34}$ ergs s⁻¹. The diffuse emission is much fainter than that in the Arches and has a very low surface brightness. It also has essentially the same spectral shape as the integrated spectrum from the detected sources. Considering the distance to the cluster, contamination by unresolved point-sources may be an issue.

Wang et al. (2006) analyze a deeper *Chandra* exposure. They report the same concerns as Law & Yusef-Zadeh (2004) and in addition note that the extent of the diffuse emission from the Quintuplet cluster is uncertain. With an extraction radius of 1 arcmin, Wang et al. (2006) find that a single-temperature thermal plasma model yields $kT = 10_{-2.7}^{+4.6}$ keV and $N_H = 3.8_{-0.5}^{+0.7} \times 10^{22}$ cm⁻², giving an absorption-corrected 2 – 8 keV luminosity of $L_x \sim 3 \times 10^{33}$ ergs s⁻¹. The radial diffuse X-ray intensity profile falls off more rapidly than SPH simulations (Rockefeller et al. 2005) predict.

A7 Westerlund 1

Westerlund 1 (hereafter W 1) is the most massive stellar cluster known in the Galaxy (Clark et al. 2005; Brandner et al. 2008). It contains a rich population of massive stars which include more than 20 WR stars (Crowther et al. 2006), more than 80 OB stars, and short-lived transitional objects including luminous blue variables (LBVs), red supergiants (RSGs) and half the currently known population of yellow hypergiants (YHGs) in the Galaxy. Estimates for its age range from 3.6 ± 0.7 Myr (Brandner et al. 2008) to 5 ± 1 Myr (Lim et al. 2013). Its distance remains somewhat uncertain, but estimates appear to be converging on the range 4 – 5 kpc (see Brandner et al. 2008, and references therein). It shows evidence of mass segregation (Lim et al. 2013).

At an age of $\sim 4 - 5$ Myr, perhaps 100 SNe have already occurred in W 1 (see, e.g., the discussion in Muno et al. 2006). The presence of an isolated X-ray pulsar confirms that supernovae have occurred there. However, the likelihood of a recent SNR contributing to the diffuse emission depends on the recent occurrence of a SN event in or near the core, as discussed in Muno et al. (2006) and Kavanagh et al. (2011).

The X-ray point sources from a *Chandra* observation are analyzed and reported by Clark et al. (2008), while the diffuse emission is analyzed by Muno et al. (2006). The diffuse emission has an intrinsic (2 – 8 keV) luminosity of $L_x \sim 3 \pm 1 \times 10^{34}$ ergs s⁻¹, and a Lorentzian spatial distribution with a HWHM along the major axis of 25 ± 1 arcseconds (~ 0.5 pc), and a 5 arcmin halo. The emission (in the energy range 1.5 – 8 keV) can be fitted with a soft thermal component ($kT_1 \sim 0.7$ keV), plus either a harder thermal component ($kT_2 \sim 3$ keV) with a low ($\lesssim 0.3$ solar) Fe abundance, or a nonthermal component with a power-law index $\Gamma \sim 2$. The absorbing column, $N_H \sim 2 \times 10^{22}$ cm⁻². In the thermal model, kT_2 increases with distance from the cluster, while in the non-thermal model, Γ is signifi-

cantly steeper in the centre-most region considered. There is no evidence for a recent SN explosion. Less than 10^{-5} of the mechanical luminosity is dissipated as 2 – 8 keV X-rays so it is conjectured that a large fraction escapes into the ISM. However, the X-ray halo between 2 – 5 arcmin (3 – 7 pc radius) is observed to attain a constant surface brightness of $\approx 7 \times 10^{-14}$ ergs cm^{-2} s^{-1} arcmin^{-2} , which is not consistent with a cluster wind where almost all of the diffuse X-ray emission is produced within the core radius R_c (Stevens & Hartwell 2003). A thermal interpretation of the halo of diffuse emission is further challenged by the high temperature and lack of line emission.

More recently, Kavanagh et al. (2011) analyze an XMM-Newton pointing and determine that the hard component in an inner 2 arcmin radius region is actually thermal, with a clearly detected He-like Fe 6.4 keV line. No evidence of a non-thermal component was found. They report that the diffuse emission has a 2 – 8 keV luminosity of $L_x \sim 1.7 \times 10^{33}$ ergs s^{-1} .

A8 The Lagoon Nebula (M8, NGC 6530)

The Lagoon Nebula is an HII region associated with the young (13 Myr) open cluster NGC 6530, which contains several O-stars and about 60 B-stars. It is about 1.3 kpc away (see Henderson & Stassun 2012, and references therein). Ongoing star formation occurs in several places, notably the Hourglass Nebula (the brightest part of M8) and M8 E. The Hourglass Nebula is illuminated by an O7V star (Herschel 36). Henderson & Stassun (2012) argue that NGC 6530 is slightly younger than the Orion Nebula Cluster (ONC), being $\lesssim 1.65$ Myr assuming the ONC is 2 Myr old. If the ONC is actually 3 Myr old, this would give the Hourglass Nebula an age of 2.5 Myr. The Lagoon Nebula is summarized in Tothill et al. (2008).

Rauw et al. (2002) claim that soft diffuse emission was “probably” detected from the southern lobe of the Hourglass nebula. The emission can be fitted with an absorbed MEKAL model with $N_H = 1.11_{-0.17}^{+0.15} \times 10^{22}$ cm^{-2} , $kT = 0.63_{-0.05}^{+0.07}$ keV and an intrinsic (0.2 – 2.0 keV) luminosity of 6.6×10^{32} ergs s^{-1} . However, there is undoubtedly some contamination from unresolved point sources. No diffuse emission is seen from a qualitative examination of a *Chandra* observation of M8 which did not cover the Hourglass Nebula (Townesley et al. 2003) - see also Damiani et al. (2004).

A9 The Arches Cluster

The Arches cluster, like the Quintuplet cluster, lies close to the Galactic Centre, being only 26 pc away in projection (see, e.g. Figer et al. 1999b). It is slightly younger (2 – 2.5 Myrs, Najarro et al. 2004; Martins et al. 2008) and more massive (Figer et al. 2002) than the Quintuplet cluster. Clarkson et al. (2012) have recently measured the kinematic mass of the cluster using *Keck*-LGS adaptive optics.

The deepest *Chandra* observation to date is by Wang et al. (2006). Diffuse thermal X-ray emission with a prominent Fe K α 6.7 keV emission line is seen from the core of the Arches cluster. The surface intensity declines steeply with radius, consistent with a cluster wind origin. This central ($r < 0.6$ pc) “plume” region can be fitted with a single temperature NEI plasma model with $kT = 2.56$ keV,

$\tau = 1.2 \times 10^{11}$ cm^{-3} s, $N_H = 1.1 \times 10^{23}$ cm^{-2} and an intrinsic (2-8 keV) luminosity of $L_x = 3.8 \times 10^{33}$ ergs s^{-1} .

In contrast, the emission in the outer regions of the cluster shows a prominent line at 6.4 keV, a power-law continuum emission of non-thermal origin, and a non-axisymmetric spatial distribution with a bowshock morphology. This may result from an ongoing collision between the cluster and the adjacent molecular cloud, which has a relative velocity of 120 km s^{-1} . The interpretation of the 6.4 keV Fe K α fluorescence emission from neutral Fe is still debated, with Wang et al. (2006) favouring a cosmic ray origin but Capelli et al. (2011) favouring photoionization of nearby molecular clouds by X-ray photons. Wang et al. (2006) find that the SE extension (which is where the 6.4 keV emission is) is best fitted with a PL+Gaussian spectral model with $\Gamma = 1.3_{-1.1}^{+1.4}$ and $N_H = 6.2 \times 10^{22}$ cm^{-2} , and has an intrinsic (2 – 8 keV) luminosity $L_x = 4.1 \times 10^{33}$ ergs s^{-1} . An even more extended “LSBXE” region is fitted with a MEKAL+PL+GAUSSIAN spectral model with $kT = 0.45$ keV, $\Gamma = 1.3$ (fixed) and $N_H = 9.2 \times 10^{22}$ cm^{-2} , with an intrinsic (2 – 8 keV) $L_x = 1.2 \times 10^{34}$ ergs s^{-1} .

Fig. 15 in Wang et al. (2006) shows the radial diffuse X-ray intensity profiles around the Arches cluster. It falls off much less rapidly than simulations (Rockefeller et al. 2005).

A10 NGC 3576 (RCW 57)

NGC 3576 is a giant HII region located at a distance of 2.8 \pm 0.3 kpc (Figuerêdo et al. 2002), and which is projected to within 30 arcminutes of the more distant region NGC 3603. Together these regions make up the RCW 57 complex. The ionizing cluster for NGC 3576 remains deeply embedded in the centre of an extended filamentary dust cloud, and not enough massive stars have yet been found to account for the radio luminosity (Figuerêdo et al. 2002; Barbosa et al. 2003).

The evidence for sequential star formation in NGC 3576 remains controversial (see Purcell et al. 2009, and references therein). These authors provide a schematic of the region (their Fig. 16).

Townesley et al. (2011) analyzed two *Chandra* pointings. A southern pointing was centered on NGC 3576, while a northern pointing was designed to search for a young stellar cluster associated with the O8V+O8V eclipsing binary HD 97484 (EM Car) and the O9.5Ib star HD 97319. Diffuse emission is seen to the SE of NGC 3576 (hereafter identified as NGC 3576S), while hard X-rays were seen in the northern pointing. Townesley et al. (2011) identified these sources as NGC 3576S and NGC 3576N, respectively. The northern pointing revealed a young cluster (termed NGC 3576OB) which appears older than NGC 3576 to the south.

NGC 3576S requires a 2-temperature spectral fit, with $kT_1 = 0.31_{-0.07}^{+0.06}$ and $kT_2 = 0.53$. The absorbing columns are $N_H = 1.3 \times 10^{22}$ cm^{-2} and $N_H = 2.5 \times 10^{21}$ cm^{-2} , respectively. The softer component dominates the total emission which has an intrinsic $L_x = 1.1 \times 10^{34}$ ergs s^{-1} . Townesley et al. (2011) suggests that the hot plasma responsible for this emission has forced itself out through a low-density pathway, analogous to the outflow seen from M17, but seen more face-on and at a slightly earlier phase. A gaussian at 0.72 keV (which accounts for 16% of the total emis-

sion) is required for a good fit. This may represent charge exchange processes.

In contrast NGC 3576N requires the presence of a power-law component in spectral models. The intrinsic luminosity is $L_x = 1.2 \times 10^{34}$ ergs s⁻¹, 24% of which is contributed by a power-law continuum. A 3-temperature model is also required for a good fit, with the hardest NEI component ($kT_3 = 0.7$ keV) accounting for 48% of the total emission. Townsley et al. (2011) speculate that the diffuse emission from this region has been enhanced by a recent cavity SN. There is no evidence for charge exchange.

A11 NGC 3603

The luminous giant HII region NGC 3603 contains the compact star cluster HD 97950, which is one of the most massive young star clusters in the Milky Way. It contains 3 core H-burning WN-stars and up to 50 O-stars (Drissen et al. 1995). The most massive stars in the core appear to be coeval with an age of about 1 Myr, while less massive stars and stars in the cluster outskirts appear to be older (Melena et al. 2008; Pang et al. 2013, and references therein). It shows clear mass segregation, despite its young age. Pang et al. (2013) suggest that dynamical processes may have been dominant for the high mass stars. Star formation appears to have occurred almost instantaneously, with Kudryavtseva et al. (2012) deriving an upper limit to the age spread of 0.1 Myr. The distance to NGC 3603 is thought to be 7 ± 1 kpc (Harayama et al. 2008). Banerjee & Kroupa (2013) explore whether a phase of substantial gas-expulsion has occurred in NGC 3603.

A *Chandra* cycle 1 observation was presented by Moffat et al. (2002), who noted diffuse X-ray emission within a central region of 2 arcmin radius with an intrinsic luminosity $L_x = 2 \times 10^{34}$ ergs s⁻¹. However, this is 20% of the integrated point source emission within this region and may be completely due to undetected point sources.

Townsley et al. (2011) recently re-analyzed this observation, finding 1328 point sources compared to the 348 sources found by Moffat et al. (2002). The diffuse X-ray emission is anti-coincident with the mid-IR emission which traces the surrounding heated dust. This is consistent with the hot plasma from the shocked stellar winds filling the cavities that they have carved. Excluding an area around the core of NGC 3603 (which is likely dominated by unresolved point sources) and a region to the west (which may contain foreground emission related to the NGC 3576 cluster), the diffuse X-ray emission is dominated by an NEI thermal plasma component with $kT_1 = 0.53$ keV, $\tau = 2 \times 10^{10}$ cm⁻³ s, $N_H = 2 \times 10^{22}$ cm⁻², and which contributes 86% of the total intrinsic $L_x = 2.6 \times 10^{35}$ ergs s⁻¹. No evidence for charge exchange processes was found though the exposure is quite short.

A12 NGC 2024 (The Flame Nebula)

The Flame Nebula, NGC 2024, is one of the nearest sites of massive star formation ($D = 415$ pc, Anthony-Twarog 1982). It is part of the Orion B giant molecular cloud (e.g. Mitchell et al. 2001) and is near the Horsehead Nebula. A 3D structure of the region was proposed by Barnes et al.

(1989) (see also Emprechtinger et al. 2009). Bik et al. (2003) suggested that the O8V-B2V star IRS 2b is the ionizing source of the HII region, but Burgh et al. (2012) note that it could be a supergiant. The age of NGC 2024 is unclear, with estimates ranging from 0.3 Myr (Meyer 1996) to several Myr (Comeron et al. 1996).

Diffuse X-ray emission with a radius of 0.5 pc from the centre of NGC 2024 was reported by Ezoe et al. (2006b). The emission has a very hard continuum ($kT > 8$ keV) and shows a He-like Fe K α line. Fitting the data with a “leaky absorber” model (where emission from a single temperature plasma reaches the observer via two paths with different absorption) returns $kT \approx 11$ keV with $N_H = 0.21 \times 10^{22}$ and 3.3×10^{22} cm⁻². The intrinsic X-ray luminosity in the 0.5–7 keV band is $L_x = 2 \times 10^{31}$ ergs s⁻¹. Ezoe et al. (2006b) note that a single massive star with a wind comparable to, or stronger than, that of a typical B0.5V star has enough energetics to power the observed X-ray emission. This work shows that diffuse emission is present in a MSFR in which only late O to early B stars exist.

REFERENCES

- Aharonian F., Akhperjanian A. G., Bazer-Bachi A. R., Beilicke M., Benbow et al., 2007, *A&A*, 467, 1075
 Anthony-Twarog B. J., 1982, *AJ*, 87, 1213
 Banerjee S., Kroupa P., 2013, *ApJ*, 764, 29
 Barbosa C. L., Damiani A., Blum R. D., Conti P. S., 2003, *AJ*, 126, 2411
 Barnes P. J., Crutcher R. M., Biegging J. H., Storey J. W. V., Willner S. P., 1989, *ApJ*, 342, 883
 Becker W., Prinz T., Winkler P. F., Petre R., 2012, *ApJ*, 755, 141
 Beuther H., Linz H., Henning T., eds, 2008, *Massive Star Formation: Observations Confront Theory Vol. 387 of Astronomical Society of the Pacific Conference Series*
 Bik A., Lenorzer A., Kaper L., Comeron F., Waters L. B. F. M., de Koter A., Hanson M. M., 2003, *A&A*, 404, 249
 Blair W. P., Morse J. A., Raymond J. C., Kirshner R. P., Hughes J. P., Dopita M. A., Sutherland R. S., Long K. S., Winkler P. F., 2000, *ApJ*, 537, 667
 Brandner W., Clark J. S., Stolte A., Waters R., Negueruela I., Goodwin S. P., 2008, *A&A*, 478, 137
 Broos P. S., Feigelson E. D., Townsley L. K., Getman K. V., Wang J., Garmire G. P., Jiang Z., Tsuboi Y., 2007, *ApJS*, 169, 353
 Burgh E. B., France K., Snow T. P., 2012, *ApJL*, 756, L6
 Canizares C. R., Winkler P. F., 1981, *ApJL*, 246, L33
 Cantó J., Raga A. C., Rodríguez L. F., 2000, *ApJ*, 536, 896
 Capelli R., Warwick R. S., Porquet D., Gillessen S., Predehl P., 2011, *A&A*, 530, A38
 Carraro G., Turner D., Majaess D., Baume G., 2013, *A&A*, 555, A50
 Castor J., McCray R., Weaver R., 1975, *ApJL*, 200, L107
 Celnik W. E., 1985, *A&A*, 144, 171
 Chevalier R. A., 2005, *ApJ*, 619, 839
 Chevalier R. A., Clegg A. W., 1985, *Nature*, 317, 44
 Chini R., Hoffmeister V., 2008, *Star Formation in M17*. p. 625

- Chu Y.-H., Chang H.-W., Su Y.-L., Mac Low M.-M., 1995, *ApJ*, 450, 157
- Chu Y.-H., Mac Low M.-M., 1990, *ApJ*, 365, 510
- Churchwell E., Whitney B. A., Babler B. L., Indebetouw R., Meade M. R., et al., 2004, *ApJS*, 154, 322
- Clark J. S., Negueruela I., Crowther P. A., Goodwin S. P., 2005, *A&A*, 434, 949
- Clark P. C., Bonnell I. A., Klessen R. S., 2008, *MNRAS*, 386, 3
- Clarkson W. I., Ghez A. M., Morris M. R., Lu J. R., Stolte A., McCrady N., Do T., Yelda S., 2012, *ApJ*, 751, 132
- Comeron F., Rieke G. H., Rieke M. J., 1996, *ApJ*, 473, 294
- Crowther P. A., Hadfield L. J., Clark J. S., Negueruela I., Vacca W. D., 2006, *MNRAS*, 372, 1407
- Damiani F., 2010, in de Grijs R., Lépine J. R. D., eds, *IAU Symposium Vol. 266 of IAU Symposium, X-rays from young star clusters: a complement to optical and infrared views*. pp 190–202
- Damiani F., Flaccomio E., Micela G., Sciortino S., Harnden Jr. F. R., Murray S. S., 2004, *ApJ*, 608, 781
- Dorland H., Montmerle T., 1987, *A&A*, 177, 243
- Dorland H., Montmerle T., Doom C., 1986, *A&A*, 160, 1
- Drissen L., Moffat A. F. J., Walborn N. R., Shara M. M., 1995, *AJ*, 110, 2235
- Dubner G., Loiseau N., Rodríguez-Pascual P., Smith M. J. S., Giacani E., Castelletti G., 2013, *A&A*, 555, A9
- Dunne B. C., Chu Y.-H., Chen C.-H. R., Lowry J. D., Townsley L., Gruendl R. A., Guerrero M. A., Rosado M., 2003, *ApJ*, 590, 306
- Dyson J. E., de Vries J., 1972, *A&A*, 20, 223
- Elmegreen B. G., Lada C. J., Dickinson D. F., 1979, *ApJ*, 230, 415
- Emprechtinger M., Wiedner M. C., Simon R., Wieching G., Volgenau N. H., Biellau F., Graf U. U., Güsten R., Honingh C. E., Jacobs K., Rabanus D., Stutzki J., Wyrowski F., 2009, *A&A*, 496, 731
- Eriksen K. A., Morse J. A., Kirshner R. P., Winkler P. F., 2001, in Holt S. S., Hwang U., eds, *Young Supernova Remnants Vol. 565 of American Institute of Physics Conference Series, Fabry-Perot [O III] λ 5007 Å observations of the SMC oxygen-rich SNR 1E 0102-72.9*. pp 193–196
- Ezoe Y., Hamaguchi K., Gruendl R. A., Chu Y.-H., Petre R., Corcoran M. F., 2009, *PASJ*, 61, 123
- Ezoe Y., Kokubun M., Makishima K., Sekimoto Y., Matsuzaki K., 2006a, *ApJ*, 638, 860
- Ezoe Y., Kokubun M., Makishima K., Sekimoto Y., Matsuzaki K., 2006b, *ApJL*, 649, L123
- Figer D. F., Kim S. S., Morris M., Serabyn E., Rich R. M., McLean I. S., 1999a, *ApJ*, 525, 750
- Figer D. F., McLean I. S., Morris M., 1999b, *ApJ*, 514, 202
- Figer D. F., Najarro F., Gilmore D., Morris M., Kim S. S., Serabyn E., McLean I. S., Gilbert A. M., Graham J. R., Larkin J. E., Levenson N. A., Teplitz H. I., 2002, *ApJ*, 581, 258
- Figuerêdo E., Blum R. D., Damineli A., Conti P. S., 2002, *AJ*, 124, 2739
- Flanagan K. A., Canizares C. R., Dewey D., Houck J. C., Fredericks A. C., Schattenburg M. L., Markert T. H., Davis D. S., 2004, *ApJ*, 605, 230
- Fujita Y., Hayashida K., Takahashi H., Takahara F., 2009, *PASJ*, 61, 1229
- Gaensler B. M., Wallace B. J., 2003, *ApJ*, 594, 326
- Gaetz T. J., Butt Y. M., Edgar R. J., Eriksen K. A., Plucinsky P. P., Schlegel E. M., Smith R. K., 2000, *ApJL*, 534, L47
- Ghavamian P., Long K. S., Blair W. P., Park S., Fesen R., Gaensler B. M., Hughes J. P., Rho J., Winkler P. F., 2012, *ApJ*, 750, 39
- Gonzalez M., Safi-Harb S., 2003, *ApJL*, 583, L91
- Gray W. J., Scannapieco E., 2011, *ApJ*, 733, 88
- Güdel M., Briggs K. R., Montmerle T., Audard M., Rebull L., Skinner S. L., 2008, *Science*, 319, 309
- Hanson M. M., Howarth I. D., Conti P. S., 1997, *ApJ*, 489, 698
- Harayama Y., Eisenhauer F., Martins F., 2008, *ApJ*, 675, 1319
- Harper-Clark E., Murray N., 2009, *ApJ*, 693, 1696
- Henderson C. B., Stassun K. G., 2012, *ApJ*, 747, 51
- Hensberge H., Pavlovski K., Verschueren W., 2000, *A&A*, 358, 553
- H.E.S.S. Collaboration et al., 2011, *A&A*, 525, A46
- Hoffmeister V. H., Chini R., Scheyda C. M., Schulze D., Watermann R., Nürnberger D., Vogt N., 2008, *ApJ*, 686, 310
- Hughes J. P., 1987, *ApJ*, 314, 103
- Hughes J. P., 1988, in Roger R. S., Landecker T. L., eds, *IAU Colloq. 101: Supernova Remnants and the Interstellar Medium X-Ray Observations of SNR EO102.2-72.2 in the SMC*. p. 125
- Hughes J. P., Rakowski C. E., Decourchelle A., 2000, *ApJL*, 543, L61
- Hughes J. P., Singh K. P., 1994, *ApJ*, 422, 126
- Hughes J. P., Slane P. O., Park S., Roming P. W. A., Burrows D. N., 2003, *ApJL*, 591, L139
- Hwang U., Canizares C. R., Markert T. H., Hughes J. P., 1992, in *American Astronomical Society Meeting Abstracts #180 Vol. 24 of Bulletin of the American Astronomical Society, High-Resolution X-Ray Spectroscopy of the Supernova Remnant N132D*. p. 790
- Hwang U., Petre R., Flanagan K. A., 2008, *ApJ*, 676, 378
- Hyodo Y., Tsujimoto M., Hamaguchi K., Koyama K., Kitamoto S., Maeda Y., Tsuboi Y., Ezoe Y., 2008, *PASJ*, 60, 85
- Katsuda S., Mori K., Tsunemi H., Park S., Hwang U., Burrows D. N., Hughes J. P., Slane P. O., 2008, *ApJ*, 678, 297
- Kavanagh P. J., Norci L., Meurs E. J. A., 2011, *New Astr.*, 16, 461
- Kim S., Staveley-Smith L., Dopita M. A., Sault R. J., Freeman K. C., Lee Y., Chu Y.-H., 2003, *ApJS*, 148, 473
- Kleinmann D. E., 1973, *Astrophys. Lett.*, 13, 49
- Koenig X. P., Leisawitz D. T., Benford D. J., Rebull L. M., Padgett D. L., Assef R. J., 2012, *ApJ*, 744, 130
- Kudryavtseva N., Brandner W., Gennaro M., Rochau B., Stolte A., Andersen M., Da Rio N., Henning T., Tognelli E., Hogg D., Clark S., Waters R., 2012, *ApJL*, 750, L44
- Law C., Yusef-Zadeh F., 2004, *ApJ*, 611, 858
- Liermann A., Hamann W.-R., Oskinova L. M., 2012, *A&A*, 540, A14
- Lim B., Chun M.-Y., Sung H., Park B.-G., Lee J.-J., Sohn S. T., Hur H., Bessell M. S., 2013, *AJ*, 145, 46
- Martins F., Hillier D. J., Paumard T., Eisenhauer F., Ott T., Genzel R., 2008, *A&A*, 478, 219
- Martins F., Mahy L., Hillier D. J., Rauw G., 2012, *A&A*, 538, A39

- Meixner M., Haas M. R., Tielens A. G. G. M., Erickson E. F., Werner M., 1992, *ApJ*, 390, 499
- Melena N. W., Massey P., Morrell N. I., Zangari A. M., 2008, *AJ*, 135, 878
- Mewe R., Kaastra J. S., Liedahl D. A., 1995, *Legacy*, 6, 16
- Meyer M. R., 1996, *PASP*, 108, 380
- Mitchell G. F., Johnstone D., Moriarty-Schieven G., Fich M., Tothill N. F. H., 2001, *ApJ*, 556, 215
- Moffat A. F. J., Corcoran M. F., Stevens I. R., Skalkowski G., Marchenko S. V., Mücke A., Ptak A., Koribalski B. S., Brenneman L., Mushotzky R., Pittard J. M., Pollock A. M. T., Brandner W., 2002, *ApJ*, 573, 191
- Morse J. A., Winkler P. F., Kirshner R. P., 1995, *AJ*, 109, 2104
- Muno M. P., Law C., Clark J. S., Dougherty S. M., de Grijs R., Portegies Zwart S., Yusef-Zadeh F., 2006, *ApJ*, 650, 203
- Nagata T., Woodward C. E., Shure M., Pipher J. L., Okuda H., 1990, *ApJ*, 351, 83
- Najarro F., Figer D. F., Hillier D. J., Kudritzki R. P., 2004, *ApJL*, 611, L105
- Oey M. S., 1996, *ApJ*, 467, 666
- Oskinova L. M., Gruendl R. A., Ignace R., Chu Y.-H., Hamann W.-R., Feldmeier A., 2010, *ApJ*, 712, 763
- Pang X., Grebel E. K., Allison R. J., Goodwin S. P., Altmann M., Harbeck D., Moffat A. F. J., Drissen L., 2013, *ApJ*, 764, 73
- Park B.-G., Sung H., 2002, *AJ*, 123, 892
- Park S., Hughes J. P., Slane P. O., Burrows D. N., Gaensler B. M., Ghavamian P., 2007, *ApJL*, 670, L121
- Parkin E. R., Pittard J. M., 2010, *MNRAS*, 406, 2373
- Pellegrini E. W., Baldwin J. A., Brogan C. L., Hanson M. M., Abel N. P., Ferland G. J., Nemala H. B., Shaw G., Troland T. H., 2007, *ApJ*, 658, 1119
- Pittard J. M., 2011, *MNRAS*, 411, L41
- Pittard J. M., Parkin E. R., 2010, *MNRAS*, 403, 1657
- Povich M. S., Churchwell E., Biegging J. H., Kang M., Whitney B. A., Brogan C. L., Kulesa C. A., Cohen M., Babler B. L., Indebetouw R., Meade M. R., Robitaille T. P., 2009, *ApJ*, 696, 1278
- Povich M. S., Stone J. M., Churchwell E., Zweibel E. G., Wolfire M. G., Babler B. L., Indebetouw R., Meade M. R., Whitney B. A., 2007, *ApJ*, 660, 346
- Purcell C. R., Minier V., Longmore S. N., André P., Walsh A. J., Jones P., Herpin F., Hill T., Cunningham M. R., Burton M. G., 2009, *A&A*, 504, 139
- Rauw G., Nazé Y., Gosset E., Stevens I. R., Blomme R., Corcoran M. F., Pittard J. M., Runacres M. C., 2002, *A&A*, 395, 499
- Raymond J. C., Smith B. W., 1977, *ApJS*, 35, 419
- Reynoso E. M., Green A. J., Johnston S., Dubner G. M., Giacani E. B., Goss W. M., 2003, *MNRAS*, 345, 671
- Rockefeller G., Fryer C. L., Melia F., Wang Q. D., 2005, *ApJ*, 623, 171
- Rodríguez L. F., González R. F., Montes G., Asiri H. M., Raga A. C., Cantó J., 2012, *ApJ*, 755, 152
- Rodríguez-González A., Cantó J., Esquivel A., Raga A. C., Velázquez P. F., 2007, *MNRAS*, 380, 1198
- Rogers H., Pittard J. M., 2013, *MNRAS*, 431, 1337
- Smith B. J., Struck C., Nowak M. A., 2005, *AJ*, 129, 1350
- Stevens I. R., Hartwell J. M., 2003, *MNRAS*, 339, 280
- Tanaka S. J., Takahara F., 2013, *MNRAS*, 429, 2945
- Tothill N. F. H., Gagné M., Stecklum B., Kenworthy M. A., 2008, *The Lagoon Nebula and its Vicinity*. p. 533
- Townsley L., Feigelson E., Montmerle T., Broos P., Chu Y.-H., Garmire G., Getman K., 2005, in Sjouwerman L. O., Dyer K. K., eds, *X-Ray and Radio Connections Parsec-Scale X-ray Flows in High-Mass Star-Forming Regions*
- Townsley L. K., Broos P. S., Chu Y.-H., Gagné M., Garmire G. P., Gruendl R. A., Hamaguchi K., Mac Low M.-M., Montmerle T., Nazé Y., Oey M. S., Park S., Petre R., Pittard J. M., 2011, *ApJS*, 194, 15
- Townsley L. K., Feigelson E. D., Montmerle T., Broos P. S., Chu Y.-H., Garmire G. P., 2003, *ApJ*, 593, 874
- Wada Q., Tsujimoto M., Ebisawa K., Miller E. D., 2013, *PASJ*, 65, L2
- Wang J., Townsley L. K., Feigelson E. D., Broos P. S., Getman K. V., Román-Zúñiga C. G., Lada E., 2008, *ApJ*, 675, 464
- Wang Q. D., Dong H., Lang C., 2006, *MNRAS*, 371, 38
- Weaver R., McCray R., Castor J., Shapiro P., Moore R., 1977, *ApJ*, 218, 377
- Winkler P. F., Kirshner R. P., 1985, *ApJ*, 299, 981
- Winkler P. F., Twelker K., Reith C. N., Long K. S., 2009, *ApJ*, 692, 1489
- Winstone E., Wolk S. J., Bourke T. L., Megeath S. T., Gutermuth R., Spitzbart B., 2011, *ApJ*, 743, 166
- Winstone E., Wolk S. J., Bourke T. L., Megeath S. T., Gutermuth R., Spitzbart B., 2012, *ApJ*, 744, 126
- Woermann B., Gaylard M. J., Otrupcek R., 2000, *MNRAS*, 317, 421
- Wolk S. J., Bourke T. L., Smith R. K., Spitzbart B., Alves J., 2002, *ApJL*, 580, L161
- Wolk S. J., Bourke T. L., Vigil M., 2008, *The Embedded Massive Star Forming Region RCW 38*. p. 124
- Wolk S. J., Broos P. S., Getman K. V., Feigelson E. D., Preibisch T., Townsley L. K., Wang J., Stassun K. G., King R. R., McCaughrean M. J., Moffat A. F. J., Zinnecker H., 2011, *ApJS*, 194, 12
- Wolk S. J., Spitzbart B. D., Bourke T. L., Alves J., 2006, *AJ*, 132, 1100
- Xu Y., Moscadelli L., Reid M. J., Menten K. M., Zhang B., Zheng X. W., Brunthaler A., 2011, *ApJ*, 733, 25
- Yusef-Zadeh F., Law C., Wardle M., Wang Q. D., Fruscione A., Lang C. C., Cotera A., 2002, *ApJ*, 570, 665